RAPID PREDICTION OF LOW-BOOM AND AERODYNAMIC PERFORMANCE OF SUPERSONIC TRANSPORT AIRCRAFT USING PANEL METHODS.

by

Ted N. Giblette

A thesis submitted in partial fulfillment
of the requirements for the degree

of

MASTER OF SCIENCE

in

Mechanical Engineering

Approved:

Douglas F. Hunsaker, Ph.D. Major Professor	Stephen A. Whitmore, Ph.D. Committee Member
Robert E. Spall, Ph.D. Committee Member	Richard S. Inouye, Ph.D. Vice Provost for Graduate Studies

UTAH STATE UNIVERSITY
Logan, Utah

2019

ABSTRACT

Rapid Prediction of Low-Boom and Aerodynamic Performance of Supersonic Transport Aircraft Using Panel Methods.

by

Ted N. Giblette, Master of Science

Utah State University, 2019

Major Professor: Douglas F. Hunsaker, Ph.D.
Department: Mechanical and Aerospace Engineering

A framework of analysis tools is developed for the rapid prediction of the sonic boom loudness and aerodynamic performance of supersonic transport geometries. An outer mold line description of the geometry is generated using parametric Class/Shape Transformation surfaces. A linearized supersonic solution of the nearfield aerodynamics is obtained using a high-order panel method, specifically, the PANAIR (A502) program. Pressure signature propagation is performed using the NASA sBOOM code, which solves the augmented Burgers equations. The loudness of the pressure signature at the ground is calculated using PyLdB, a code that implements Steven's Mark VII method for perceived loudness. Grid convergence studies are used to verify the nearfield panel solution and results are benchmarked against high-fidelity solutions available from the 2017 AIAA Sonic Boom Prediction Workshop. Good agreement is found between PANAIR and Euler results except for in regions where the assumptions of weak shocks, not transonic, and small perturbation velocities are violated.

(95 pages)

PUBLIC ABSTRACT

Rapid Prediction of Low-Boom and Aerodynamic Performance of Supersonic Transport Aircraft Using Panel Methods.

Ted N. Giblette

The Utah State University Aerolab developed and tested a set of tools for rapid prediction of the loudness of a sonic boom generated by supersonic transport aircraft. This work supported a larger effort led by Texas A&M to investigate the use of adaptive aerostructures in lowering sonic boom loudness at off design conditions. Successful completion of this effort will improve the feasibility of supersonic commercial transport over land.

Funding was provided by a NASA University Leadership Initiative grant to several universities, including Utah State University, as well as industry partners to complete this work over a five year period. The work presented in this thesis was done over the first year of the grant.

The Aerolab team was specifically tasked with developing a set of tools for rapidly predicting the sonic boom loudness of supersonic aircraft. Specifically, this work included an assessment of the existing analysis tools available followed by the planning, development, and testing of a framework of tools for performing the needed calculations.

Results of the framework were compared against high fidelity solutions available from the 2017 AIAA Sonic Boom Prediction Workshop. These comparisons revealed that panel methods perform well for simple geometries. However, localized errors appear when modeling more complex geometries that reduce the accuracy of the predicted sonic boom loudness. It was found that these localized errors were a consequence of the inherent assumptions built into panel methods. Consequently, in future work, it may be necessary to develop techniques for combining the results of panel methods with higher fidelity methods or to revisit the panel method formulation.

For my family...

ACKNOWLEDGMENTS

I am incredibly grateful to all those who provided me with this opportunity, especially Dr. Douglas F. Hunsaker and those leading the ULI grant at Texas A&M, and to my God for guiding me to the opportunity and sustaining me through it. I am especially grateful to my wife who never stops believing in me and who's support never waivers and to my beautiful children for always lifting my spirits when I need a break. A big thanks to Matthew Smith (Boeing) and Stephen Smith (retiree of NASA Ames) who so generously gave of their time and expertise.

This work is supported by the NASA *University Leadership Initiative* (ULI) program under federal award number NNX17AJ96A, titled "Adaptive Aerostructures for Revolutionary Civil Supersonic Transportation".

Ted N. Giblette

CONTENTS

LIST OF TABLES

LIST OF FIGURES

CHAPTER 1

INTRODUCTION

The disturbances caused by sonic booms are a major barrier to the use of supersonic transport aircraft. Aircraft traveling at supersonic speeds cause shock waves that correspond to abrupt changes in the properties of the air such as pressure, density and temperature. These shock waves travel out and away from the aircraft and down to the ground where the rapid pressure changes in the air cause an audible noise often referred to as a sonic boom. In addition to the noise of the sonic boom, these pressure changes can cause other disturbances such as rattling windows and, if severe enough, structural or environmental damage. As a result of the noise and potential hazards, supersonic travel over land has been restricted, such as in the Code of Federal Regulations (CFR) 91.817 in the United States [1]. Overcoming the barrier that the sonic boom poses to supersonic flight requires the ability to understand and model the shock wave generation and propagation and the resulting sonic boom.

The initial theories and models developed for shock wave propagation predict that, at large propagation distances, all shock waves asymptotically approach the characteristic N-wave shape shown in Fig. 1.1 regardless of initial shape [2]. Thus, it appeared that the pressure disturbance at the ground was mostly independent of the shape of the aircraft and that little could be done to overcome this obstacle. However, in 1965, F. Edward McLean showed that the shock waves from large supersonic aircraft have often not yet reached a fully asymptotic state upon arrival at the ground [3]. Thus, the shape of the shock wave at the ground and the resulting disturbance can be controlled by changing the shape of the aircraft. Since then, many studies have been performed that investigate optimal aircraft shapes for minimizing the disturbance at the ground.

Although significant progress has been made over the last several decades [4], this progress has come slowly because of the difficult nature of the problem. Developing quiet

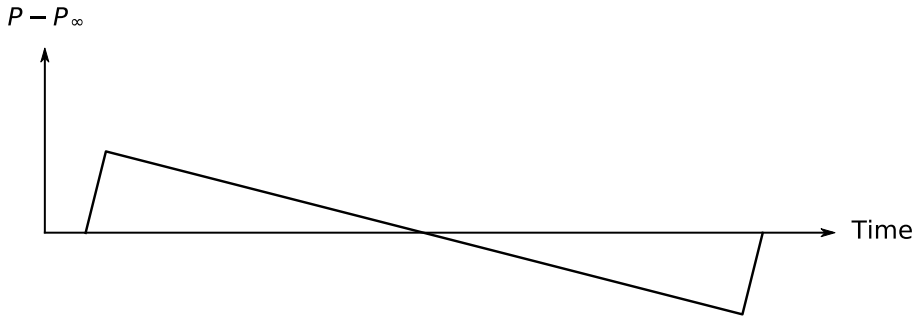

Fig. 1.1: Asymptotic N-wave pressure signature.

supersonic transport aircraft is analogous in some ways to trying to drive a speed boat across a small lake while only generating waves that have a certain shape and amplitude at the shoreline. For the case of supersonic aircraft, the aircraft must produce sufficient lift, have low levels of drag, be structurally sound, and be stable and maneuverable in addition to producing a specific shape of shock wave at the ground. Furthermore, the shape of the shock wave at the ground is a function of the altitude of the aircraft and the properties of the atmosphere between the aircraft and the ground, including the temperature, humidity, pressure, and wind.

Several supersonic transport concepts have been developed that show low-boom performance for specific flight and atmospheric conditions [5, 6]. However, this performance tends to degrade rapidly at off-design conditions [7, 8]. The present work is part of an effort involving both academic and industry partners to achieve robust low-boom performance through structurally morphing the aircraft during flight.

The aims of the present work are two-fold. First, the development of a framework of tools for the automated, rapid prediction of sonic boom loudness and aerodynamic performance to be used as part of a multidisciplinary analysis and optimization (MDAO) effort. Second, to verify solution convergence and to benchmark the solution against existing high-fidelity solutions.

The prediction of the sonic boom loudness at the ground commonly involves multiple steps/models as outlined in Fig 1.2. Once a description of the geometry is obtained, the next step is to model the air flow directly around the aircraft using an aerodynamic model.

The pressure changes caused by the shock waves generated by the aircraft can then be measured. The measured pressure changes are often referred to as the nearfield pressure signature. A wave propagation model is then used to propagate the nearfield pressure signature down to the ground. Finally, the resulting pressure signature at the ground is processed using a noise metric to yield a loudness.

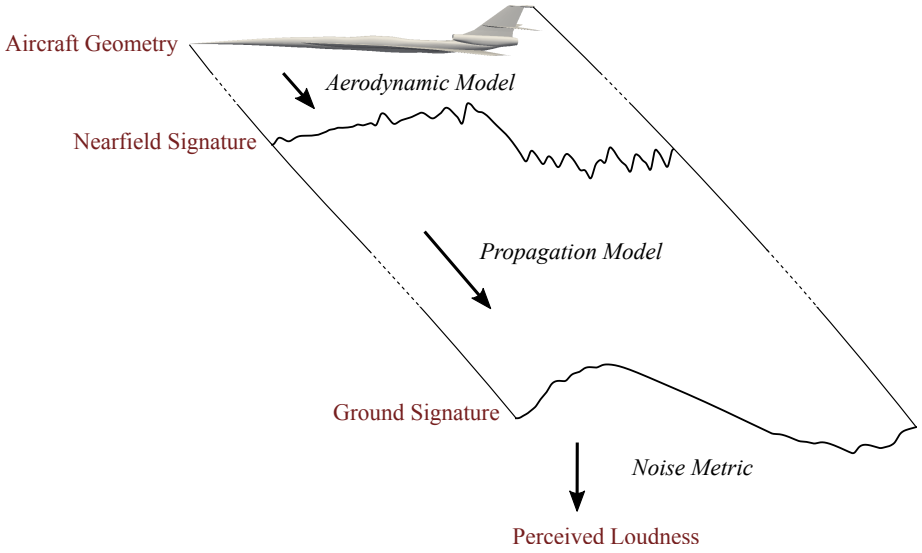

Fig. 1.2: Process for predicting sonic boom loudness.

While it is common to employ full computational fluid dynamics (CFD) to obtain the nearfield aerodynamics, this is a computationally intensive process often requiring super computers and long run times. Instead, the current work employs panel methods which are several orders of magnitude faster. Panel solutions have some limitations but still capture much of the critical physics of this problem as shown previously by others [9–11]. It is expected that, with faster run times, this framework will be able to explore a broad design space and inform subsequent, narrower, high-fidelity studies.

An important step in achieving the goals of the current work is understanding the accuracy of the models used inside it. Grid convergences studies provide model verification as well as insight into the grid refinement necessary to balance performance and accuracy. The recent 2017 AIAA Sonic Boom Prediction Workshop has provided a wealth of data for

several supersonic geometries [12]. This allows the current framework to be benchmarked against cutting edge, high-fidelity results from many prominent researchers in the field.

CHAPTER 2

LITERATURE REVIEW

This chapter summarizes the theory that provides the foundation for the present work. This summary will be divided by topic into several sections: classical sonic boom theory, modern methods for sonic boom prediction, sonic boom metrics, and sonic boom prediction frameworks and tools.

Since the sonic boom prediction touches on a broad range of topics, the information presented in this chapter focuses only on the previous work that is most relevant to the current work. For a more complete review of all the topics involved, the reader is referred to other sources [4, 13–16]. A particularly thorough coverage of much of what has been done in the past six decades is provided in [4].

2.1 Classical Sonic Boom Theory

Initial attempts to model supersonic flow focused on linearized solutions to the equations governing compressible inviscid fluid flow, hereafter referred to as linear theory. These efforts began in 1925 by developing linear theory for the two-dimensional supersonic airfoil problem in order to obtain lift, drag, and moment coefficients [17]. As time continued, the theory continued to be developed by many researchers [18–22] and was applied to geometries such as bodies of revolution [18] and delta wings [22–24]. A complete development of the linearized supersonic theory was put forward by Hayes in 1947 [25].

Although successful in modeling supersonic aerodynamic performance in many common applications, linear theory is fundamentally insufficient for predicting flow properties far away from the body. This is because supersonic flow is fundamentally nonlinear and the effects of this nonlinearity accumulate at large distances away from the body.

In order to address the shortcomings of linear theory for predicting flow properties away from the body, Whitham developed a modified linear theory [2]. The primary development

in this modified theory is the use of the actual non-linear characteristic lines in combination with the linearized governing equations. Additionally, Whitham developed an approach for approximating the location and strength of shock waves that form as the pressure waves propagate away from the body. This is done using an equal area bisection method at points where the non-linear characteristic lines intersect.

There were several important implications of Whitham's findings. First, it was shown that linear theory can provide an accurate model of the flow field far away from the body if combined with the exact non-linear characteristics. Second, Whitham showed that, despite initial shape, all shock wave patterns asymptotically approach an N-wave shape, shown in Fig. 1.1, at large distances. Thus, at very large distances, the strength of the shock depends only on the properties of the fluid, the distance from the body, and the length of the body and is independent of the particular body shape. Finally, Whitham established that similar principles would hold for non-axisymmetric bodies at distances sufficiently far from the aircraft when the cross-wise gradients due to asymmetry become small relative to axial gradients.

Whitham's work has grown into the now common nearfield-midfield-farfield paradigm [4]. This approach to the sonic boom prediction divides the domain into three parts as shown in Fig. 2.1. The nearfield extends from the aircraft out to where the cross-wise gradients are small and the pressure signature can be accurately approximated as one dimensional. This is not an immediate transition and the distance will vary based on the specific aircraft geometry. The midfield extends from where the signature can be treated as one dimensional to where it has reached the N-wave shape. At this point, referred to as the farfield, the shape of the wave is independent of the specific aircraft geometry and is no longer changing with further propagation except that the amplitude continues to decay. When divided in this way, the problem can be treated piecewise, using the models best suited to each part. Additionally, if a farfield signature is assumed, the calculation is greatly simplified.

Much of the work done in the years immediately following Whitham's 1952 paper assumed farfield signatures. It wasn't until 1965, that McLean showed that for a rep-

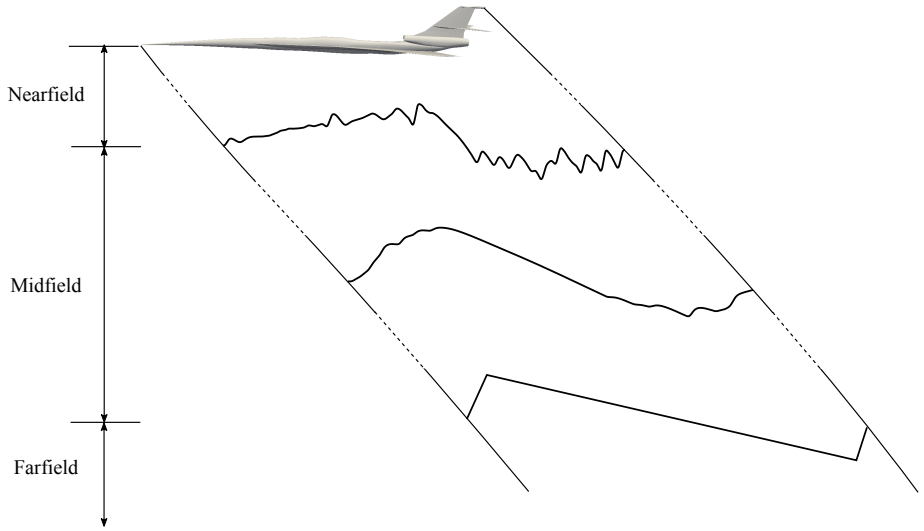

Fig. 2.1: Nearfield-midfield-farfield paradigm.

resentative supersonic transport configuration the signature wouldn't actually reach the asymptotic state until much further than a cruise altitude of 44,000 feet [3]. Additionally, The distance over which the signature would reach the asymptotic state or the length of the midfield depended on the shape of the aircraft. These findings had important implications for the supersonic community because it meant that the shape of the sonic boom signature at the ground could, in many cases, be controlled by the shape of the aircraft.

In the years following Whitham's 1952 paper, several researchers verified the accuracy of modified linear theory [26–28] and some improvements were made to the theory. In 1955, Lomax generalized modified linear theory for arbitrary lifting configurations [29] and in 1958, Walkden applied these findings to sonic boom prediction [30].

Another important step forward was the use of geometric acoustics to model how the sonic boom propagates through a non-uniform atmosphere. Researchers had been studying the propagation of sound through a non-uniform atmosphere as early as 1921 [31], but much of the major development of geometric acoustics occurred in the 1940s and 50s [32–36] along with efforts in applying the theory to the problem of sonic boom prediction [37–41].

The combination of Whitham's method and its subsequent extensions with geometric acoustics constitutes what is referred to in this work as classical sonic boom theory. A more

detailed explanation of this theory, including a systematic description of the process and corresponding equations, is provided by Plotkin [15].

Classical sonic boom theory can provide accurate predictions of the sonic boom ground signature of asymmetric, lift-producing aircraft, but the theory does have inherent limitations. Many of the limitations of classical sonic boom theory stem from its foundation in linear theory, which assumes long slender bodies and supersonic, inviscid, and irrotational flow. Other limitations include difficulties in modeling geometry using an equivalent axisymmetric representation [42], modeling shock rise times [43], and modeling effects of atmospheric turbulence [44]. As discussed in the next section, methods have been developed to supplement or replace elements of the classical theory and overcome these limitations.

2.2 Modern Methods for Sonic Boom Prediction

Increased understanding of the underlying physics and improvements in computational technology has allowed for the use of more complete models and tools in predicting the sonic boom. These improved models include full CFD solutions for the flow field near the body, propagation using the Augmented Burger's equations, and even methods for modeling the effects of atmospheric turbulence. This section provides some brief examples of some of the more prominent developments for both the nearfield solution and the pressure signature propagation.

2.2.1 Improvements in the Nearfield Solution

In order to analyze a lifting wing-body geometry using modified linear theory, the effects of lift, geometry, and the interference between the wing and body must all be modeled with an equivalent axisymmetric body of revolution [30]. This modeling process becomes increasingly difficult as the complexity of the geometry increases [42]. Additionally, modified linear theory breaks down as the Mach numbers rise above 3 [45]. As a result of these limitations and improvements in CFD methods and computational technology, researchers began to use full Euler CFD solutions to obtain the nearfield solution [46–48].

Full CFD solutions come with their own set of challenges since solutions are expensive

and become increasingly more so with increase in domain size. This cost is especially high when extending out the domain far enough as to correctly match the nearfield CFD solution with the one dimensional propagation models. As a result, techniques have been developed to match the three-dimensional nearfield solution produced by the CFD with the propagation codes [46, 49–51]. These techniques allow for a smaller domain to be used for the nearfield CFD solution. As computational technology has continued to mature rapidly and solution methods have improved, it has become common in recent years to just increase the domain size of the nearfield solution enough to provide a nearfield pressure signature that is well-approximated as one dimensional. While possible, this type of solution still comes at a high computational cost and is impractical for applications such as optimization.

Another option is to use panel methods as a compromise between obtaining quick solutions and maintaining reasonable accuracy. High-order panel methods, which were developed heavily in the 1970s and 80s, can provide a linearized inviscid supersonic solution of the nearfield flow at a computational cost that is orders of magnitude smaller than a full CFD solution [52]. Because of this cost advantage, panel methods have been used in optimization studies of low-boom supersonic transport aircraft where large numbers of solutions are required [9–11, 53].

In addition to performance, there are other trade offs when considering panel methods. Panel solutions have advantages over classical theory in that the geometry is modeled directly. Consequently, the three-dimensional effects of non-axisymmetric geometries such as lift and shielding effects are modeled without the need of determining equivalent axisymmetric bodies. However, since panel methods provide a linearized inviscid solution, they are restricted to long slender bodies, low Mach numbers, and are not able to accurately model the nearfield signature at large distances. Unlike full CFD, panel solutions can provide a nearfield solution at any distance away from the aircraft with no additional computational cost. However, because this solution is linear and assumes a uniform flow field, the error of the solution increases with distance [9]. Thus, the error due to the signature being sufficiently far away as to be safely treated as one dimensional and the error due to the

uniform atmosphere and linear assumptions of the panel method must be balanced. This balance will be investigated in the present work.

A method for correcting the error due to the linearity of the panel solution was proposed by Chan [9]. This method involves calculating the nearfield signature using a panel method, finding an equivalent axisymmetric source distribution, and then using modified linear theory, which does take into account the nonlinearity, to calculate a new nearfield signature.

It is also important to note that panel solutions are not good for flow that is transonic or near transonic. Previous research has found that the wave drag predictions provided by the panel solution have large errors when the Mach number normal to the leading edge of the wing is near transonic [9, 11].

In addition to using full CFD and panel solutions to obtain the near field solution, researchers have revisited the classical methods of modified linear theory [42]. This research investigated improvements that can be made to the classical theory and compared results to experimental data for modern supersonic aircraft.

2.2.2 Improvements in the Pressure Signature Propagation

The modified linear theory developed by Whitham allowed for the pressure signature at the ground to be calculated by hand for simple geometries and a uniform atmosphere. However, as the method was extended to more complex lifting bodies and ray tracing was used to account for the effects of a stratified atmosphere, wind, and maneuvering flight, it became necessary to develop computer programs to carry out the calculations. An early example of such a program was published in its entirety, including the FORTRAN source code, in 1969 [54].

In addition to extending modified linear theory, new methods and models have been developed for propagating the nearfield pressure signature to the ground. One method is to use the Burger's equation and extend it to include effects such as molecular relaxation and thermoviscous absorption [43, 55–57]. The primary advantage of this method over modified linear theory is the ability to accurately model shock rise-times which factor into

the calculation of the sonic boom loudness at the ground. Another method for the pressure signature propagation is to use a full potential solution coupled with an Euler CFD nearfield solution [58]. Since the full potential solution is three-dimensional, it can be coupled with the Euler solution close to the aircraft. This method is also able to account for atmospheric changes in temperature and pressure.

An important aspect of the pressure signature propagation which will not be considered in the current work is the effect of atmospheric turbulence. For more information on this subject, the reader is referred to other sources [4, 16].

2.3 Sonic Boom Metrics

Once a sonic boom pressure signature is obtained at the ground, there are several metrics which can be used to provide a measure of the sonic boom severity. Early studies investigating sonic boom minimization suggested several options, including maximum overpressure, impulse (area under the pressure-time curve), or the pressure rise through the shock [59]. Additionally, investigations have been performed into loudness as a metric [60–63].

Metrics such as maximum overpressure or impulse are easily calculated, but each by itself is incomplete when it comes to gauging human response or annoyance. In order to determine effects of the pressure signature shape on the subjective loudness, studies have been performed using sonic boom simulators and human subjects [62–65]. One of these studies determined that increasing the front shock rise time and decreasing the front shock peak amplitude generally reduced the subjective loudness [62].

Because the human response is sensitive to both the amplitudes and the associated frequencies, loudness metrics have been developed that attempt to weight the frequencies accordingly. These metrics include Steven's Mark VII perceived loudness [66] and the commonly used A-weighted and C-weighted loudness metrics [67]. Studies correlating these and other loudness metrics to the subjective loudness have shown that some of these metrics perform better than others [63, 68]. Steven's Mark VII perceived loudness or PL has been consistently shown to be a good indicator of outdoor and indoor loudness [63, 68].

In general, there is no one metric that effectively quantifies the severity of the sonic boom with respect to all of the various considerations. For example, the human response is different than a structural response and thus sensitive to different signature characteristics. The current work will only consider the human response and will use PL as the metric with units of PLdB.

2.4 Sonic Boom Prediction Frameworks and Tools

In performing optimization of supersonic aircraft configurations, a framework of tools is desired that accepts parameters describing a specific geometry and then performs the necessary steps to return aerodynamic performance coefficients and sonic boom loudness. A generic outline of such a framework is shown in Fig. 2.2. Several frameworks of this nature have been developed for low-boom aircraft optimization [9–11, 69–71].

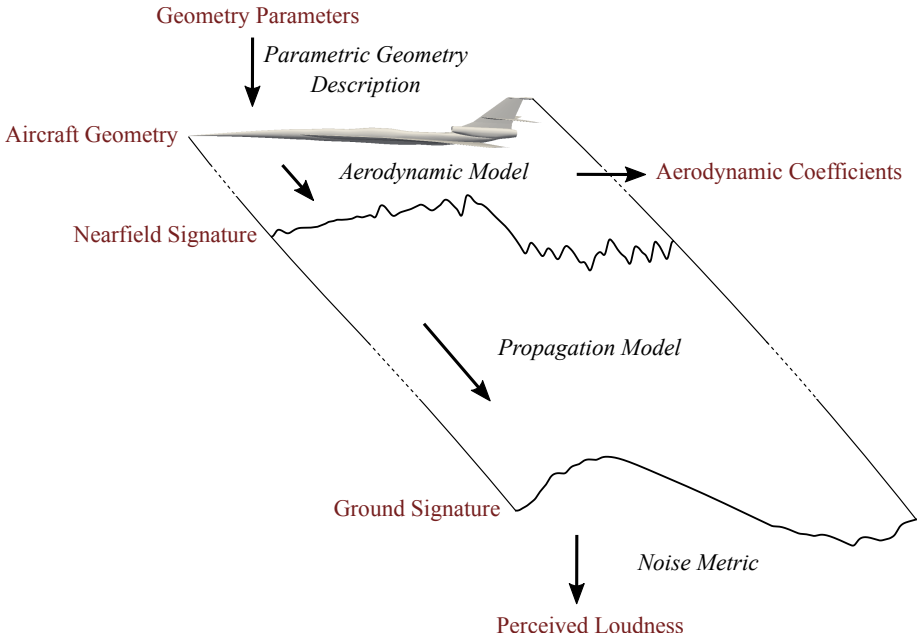

Fig. 2.2: Outline of framework for sonic boom optimization.

Rallabhandi outlined a method for combining parametric surfaces together to obtain a structured surface mesh and then combined this with a panel code and a propagation code

to predict pressure signatures at the ground [10]. The method for obtaining a structured mesh involved generating meshes for each individual surface and then using a geometry triangulation library to find the intersections. The intersection information along with predefined logic for a given wing configuration was then used to divide the surface into the networks required for the panel code.

Previous efforts that have employed high-order panel methods for sonic boom prediction [9,10,53] have all used the Boeing developed PANAIR code [72] since no other comparable public domain options exist. Although previous efforts have shown the PANAIR program to be sufficient, some undesirable limitations have been reported including, restrictions in defining the surface mesh, insufficient precision on the data, and the boundary conditions for the nacelles not working at supersonic speeds [9].

In performing the propagation of the sonic boom signatures, both classical theory and the augmented Burger's equation methods have been used [9,10]. Currently, several software tools exist that implement modern propagation algorithms at a computational cost much less than the nearfield solution. Thus, in most cases, it doesn't make sense to resort to less accurate classical methods.

One of the most prominent sonic boom propagation tools, is the NASA developed PCBoom code. PCBoom uses full ray tracing propagation theory to track the entire boom carpet including the effects of maneuvering flight, non-standard atmospheric profiles, wind, and even the focused superbooms that can occur during maneuvering flight [73]. Additionally, the effects of atmospheric absorption, diffusion, and molecular relaxation are included through frequency domain corrections. The code has also been modified to include a full three-dimensional atmosphere and ellipsoidal earth model [74]. The ability to track the entire boom carpet for a given flight path is important in planning flights that minimize impact on populated areas.

Another propagation tool is the NASA developed sBOOM. Propagation in sBOOM is done with an algorithm that handles all propagation mechanisms in the time domain [43]. This avoids the error and computational cost of the frequent Fast-Fourier Transform (FFT)

and inverse FFT operations employed in other methods. Additionally, sBOOM handles stratified atmospheres with wind and is able to predict off-track signatures and ground intersection location with respect to aircraft location. Both sBOOM and PCBoom are available through the NASA Technology Transfer Program.

CHAPTER 3

METHODS

This chapter summarizes the development of a framework of tools for generating parameterized supersonic aircraft geometries and predicting the corresponding aerodynamic performance and sonic boom loudness. As outlined in Fig. 3.1, the tools and models used for each step are as follows. A parametric geometry description is developed using the

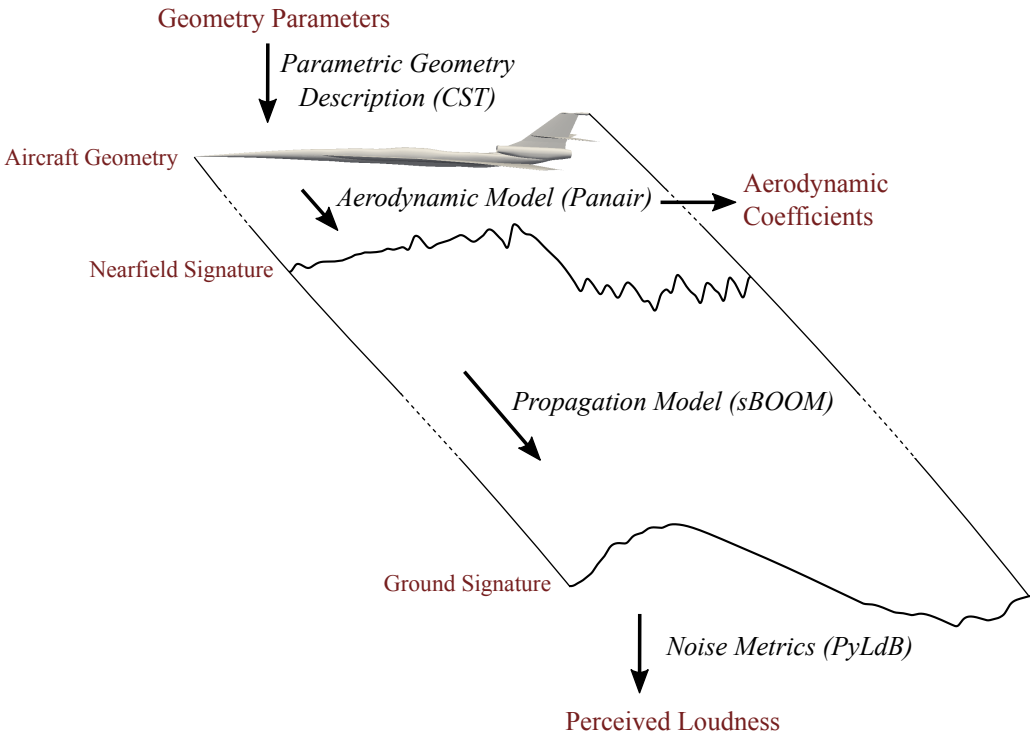

Fig. 3.1: Overview of tool framework.

Class/Shape Transformation (CST) method which, once intersections of various surfaces are found, provides a watertight and fully parameterized description of the outer mold line. With this geometry description, the structured surface mesh required by PANAIR can be generated. A PANAIR solution provides aerodynamic performance coefficients and

the nearfield pressure signature. The pressure signature is propagated to the ground using sBOOM and a corresponding loudness is calculated using PyLdB [75], a code that implements Steven's Mark VII method for calculating perceived loudness. The following sections will describe each step and the tools used in greater detail.

3.1 Geometry Description

The first component of the sonic boom prediction framework is the description of the aircraft geometry. How the geometry is parameterized affects the types of geometries achievable and will depend on the goals of the optimization study. For example, in preliminary design it is import to explore broader changes in wing sweep, twist, and taper and even different wing, tail, and nacelle configurations as done previously by others [9, 10, 69, 70]. However, the current work is different in that the objective is to look at small localized changes that can be made to an existing design. Thus, geometry description and parameterization techniques are desired that, given a baseline geometry, provide fine control over the surface.

Several methods have been developed for parameterizing geometries and studies have been performed comparing the strengths of each method [76, 77]. The CST description has been shown to reach a large portion of the desired design space (smooth geometries) with a minimal number of parameters [78]. Additionally, recent work by Leal and Hartl has shown that the CST equations can be modified to provide a structurally consistent description [79]. Consequently, the use of a CST description for supersonic geometries will be investigated in the current work.

3.1.1 Class/Shape Transformation Equations

The CST formulation was originally introduced with two forms of the three-dimensional CST equations, one set of equations for axisymmetric bodies and another for wings [78]. The current work employs an extended CST methodology which was outlined by Leal et al. [80]. This extended CST formulation provides a general set of equations that captures both fuselage and wing geometries and calculates true wing twist instead of the small angle

twist used in the original formulation.

The CST methodology provides a set of parametric equations

$$x = f_1(\psi, \eta, p_i) \tag{3.1}$$

$$y = f_2(\psi, \eta, p_i) \tag{3.2}$$

$$z = f_3(\psi, \eta, p_i) \tag{3.3}$$

that map dimensionless coordinates ψ and η, each with a range $(0, 1)$, to the physical x, y, and z coordinates of a surface. In addition to the nondimensional coordinates, each equation is also a function of several parameters p_i, which control the shape of the surface.

The behavior of the CST equations is understood most easily in two dimensions where instead of a surface, a parameterized line is generated. The CST equations in two dimensions are

$$x = \psi X \tag{3.4}$$

and

$$z = C(\psi)S(\psi)Z\,. \tag{3.5}$$

The parameters X and Z are characteristic lengths, corresponding to the length of the curve in the x-direction and height of the curve in the z-direction respectively. The functions $C(\psi)$ and $S(\psi)$ are called the class and shape functions respectively and are the primary elements of the CST methodology. The class function is defined as

$$C(\psi) = \psi^{N_1}(1 - \psi)^{N_2} \tag{3.6}$$

and controls the general shape of the curve. This can be seen by setting the shape function equal to 1 and varying the N_1 and N_2 parameters as shown in Fig. 3.2. The N_1 parameter controls the shape of the curve at values of ψ close to 0 and the N_2 parameter controls the

shape near $\psi = 1$.

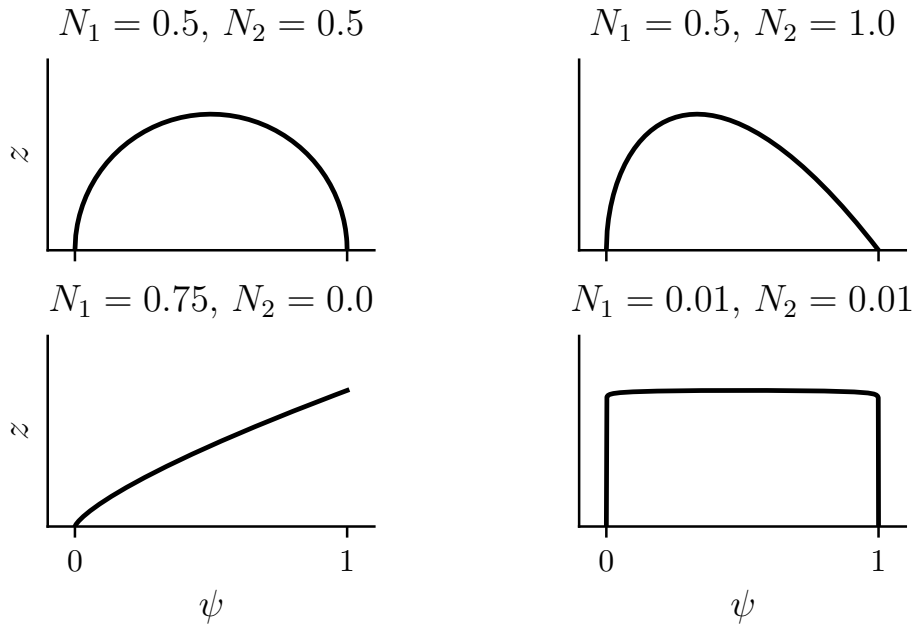

Fig. 3.2: Examples of class function.

As discussed by Leal et al. [80], a normalizing coefficient, k, can be added to the class function such that the peak always has a magnitude of 1. The class function becomes

$$C(\psi) = k\psi^{N_1}(1-\psi)^{N_2} \tag{3.7}$$

where

$$k = \frac{(N_1 + N_2)^{N_1+N_2}}{N_1^{N_1} N_2^{N_2}} \tag{3.8}$$

The shape function, $S(\psi)$, is used to fine tune the shape of the curve. For example, a class function with $N_1 = 0.5$ and $N_2 = 1.0$ gives the general shape of a low-speed airfoil with a round nose and sharp trailing edge. The shape function could then be adjusted to produce the specific geometry of a NACA 2412 or any other airfoil that fits well within the class. Kulfan uses a Bernstein polynomial for the shape function since it provides a smooth

curve and the ability to improve accuracy by increasing the order of the polynomial [78]. Bernstein polynomials are defined as

$$B_n(x) = \sum_{i=0}^{n} A_i \binom{n}{i} x^i (1-x)^{n-i} \tag{3.9}$$

where

$$\binom{n}{i} \equiv \frac{n!}{i!(n-i)!} \tag{3.10}$$

The order of the polynomial is n and the A_n terms or Bernstein coefficients are parameters that can be adjusted to achieve a specific shape of curve. An example curve is shown in Fig. 3.3 where the individual terms of the Bernstein polynomial are plotted along with the total.

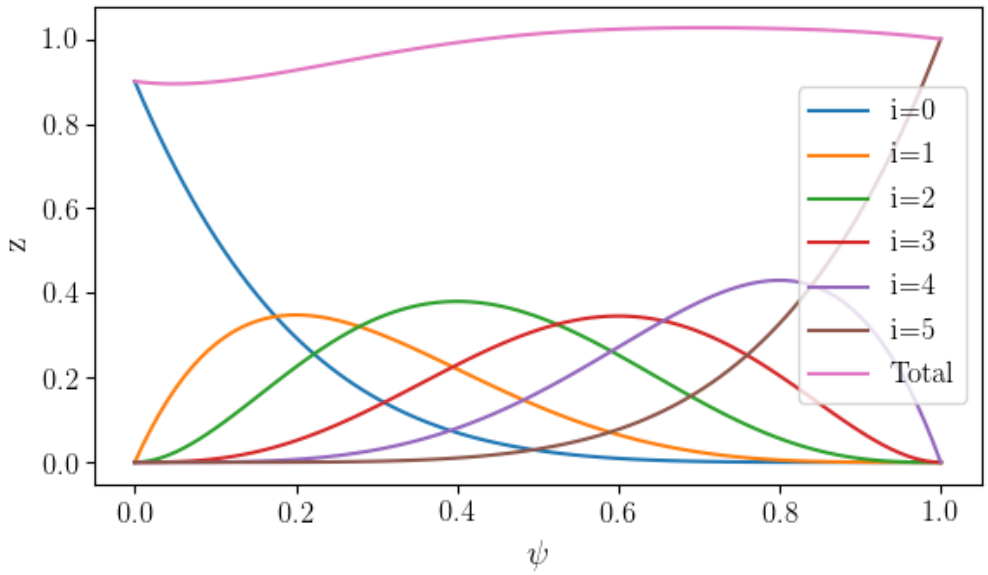

Fig. 3.3: Example of Bernstein polynomial.

As shown by Kulfan [78], using Bernstein polynomials for the shape function provides good accuracy and control for a large range of shapes. However, in some instances, it may

make sense to use something other than Bernstein polynomials for the shape function. It should also be noted that, with the addition of the shape function, the characteristic length Z is no longer equal to the max height of the curve in the z-direction. This would only be the case if the class and shape functions both had a max height of 1 at the same ψ location, which is not going to be true in general.

In order to complete the general two-dimensional CST equations, two more additions will be made. First, a z_ψ term in the z equation provides the ability to create an offset in the z-direction that varies with ψ. Second, the addition of reference values, ζ_0 and ψ_0, allow for the reference coordinate system to be shifted relative to the curve. The resulting two-dimensional CST equations are

$$x = (\psi - \psi_0)X \tag{3.11}$$

$$z = [C(\psi)S(\psi) - \zeta_0]\, Z + z_\psi(\psi) \tag{3.12}$$

The z_ψ term provides the ability to create a trailing edge gap. For example, a trailing edge gap with thickness $2\delta_{te}$ can be created by using $z_\psi = \psi\delta_{te}$ as shown in Fig. 3.4.

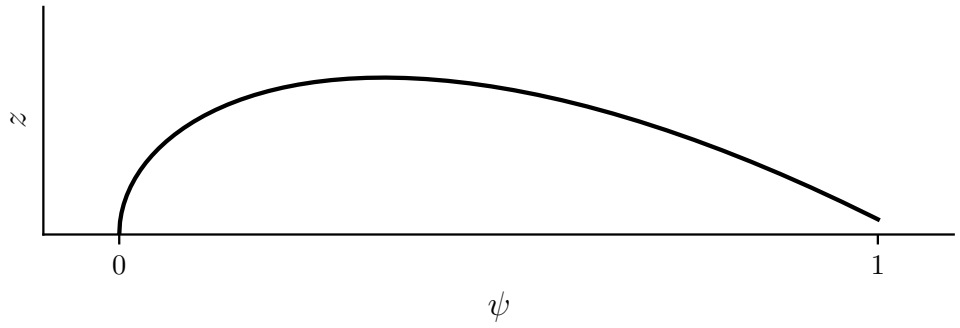

Fig. 3.4: Example of airfoil with trailing edge gap.

Using the ψ_0 and ζ_0 reference values, with a range of [0, 1], the coordinate system can be moved relative to the curve. Examples of this movement are shown in Fig. 3.5. The

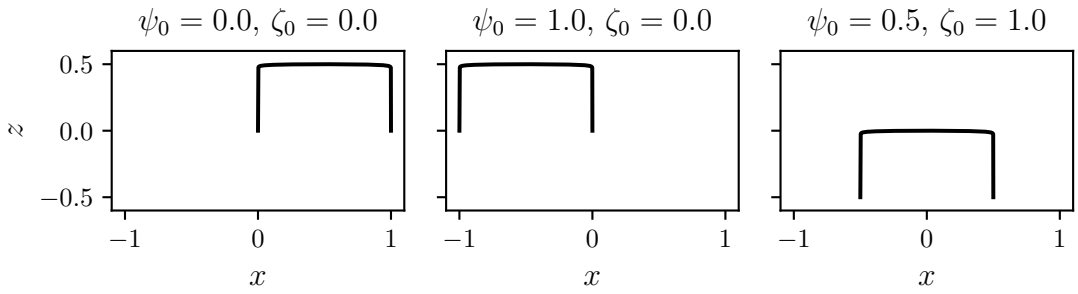

Fig. 3.5: Example of shift in reference coordinate system in 2D.

utility of this shift in the reference coordinate system will become more obvious in the full three-dimensional CST formulation.

The three-dimensional CST equations are simply an extension of the two-dimensional formulation. The three-dimensional surface consists of a continuous series of two-dimensional curves with parameters that vary in the y-direction. The general formulation used in this work is similar to that introduced by Leal et al. [80] and is

$$\begin{pmatrix} x \\ y \\ z \end{pmatrix} = \mathbf{T} \begin{pmatrix} [\psi - \psi_0]\, X(\eta) \\ [\eta - \eta_0]\, Y \\ [C(\psi,\eta)S(\psi,\eta) - \zeta_0]\, Z(\eta) + z_\psi(\psi) \end{pmatrix} + \begin{pmatrix} x_\eta(\eta) \\ 0 \\ z_\eta(\eta) \end{pmatrix} \tag{3.13}$$

where

$$\mathbf{T} = \begin{pmatrix} cos(\alpha_T(\eta)) & 0 & sin(\alpha_T(\eta)) \\ 0 & 1 & 0 \\ -sin(\alpha_T(\eta)) & 0 & cos(\alpha_T(\eta)) \end{pmatrix} \tag{3.14}$$

In addition to the two-dimensional parameters being allowed to vary along the span, this three-dimensional formulation adds several terms. The $x_\eta(\eta)$ and $z_\eta(\eta)$ terms shear the surface in the x and z directions respectively and a twist matrix, $\mathbf{T}$, rotates the two-

dimensional sections about the y-axis to obtain a washout or twist distribution, $\alpha_T(\eta)$. The Y and η_0 terms are a characteristic length and reference value respectively and perform a function similar to those found in the x and z equations. The class and shape functions are the same as in the two-dimensional case except that the class exponents and the Bernstein coefficients are now functions of η.

An example wing case helps illustrate the function of the parameters in the CST equations. Figure 3.6 shows the planform of a supersonic wing generated using the three-dimensional CST equations. In the case of a wing, $X(\eta)$ and $Z(\eta)$ are set equal to each

Fig. 3.6: Example of wing surface generated using CST equations.

other and are the chord as a function of the span. The $x_\eta(\eta)$ term is used to sweep the wing. As show in Fig. 3.7, these parameters are implemented as piecewise functions for this wing. The $z_\eta(\eta)$ term controls the dihedral of the wing. Note that dihedral is commonly defined as a solid body rotation of the wing whereas the $z_\eta(\eta)$ term shears each section upward. For small amounts of dihedral there is only a small difference between the two approaches. If the traditional definition of dihedral is desired, the wing can be rotated in the global reference frame as will be explained later in this section.

Changing the ψ_0 term shifts the reference coordinate system and changes how the sweep is defined. Figures 3.8 and 3.9 show, for the cases of 0 degrees sweep and 30 degrees sweep, how the sweep can be defined about the leading edge, quarter chord, or trailing edge.

The same three-dimensional CST equations used to generate wing geometries can also be used for fuselage geometries. For example, the class exponents can be adjusted to achieve a circular cross-section and the radius of the fuselage specified as a function of distance along

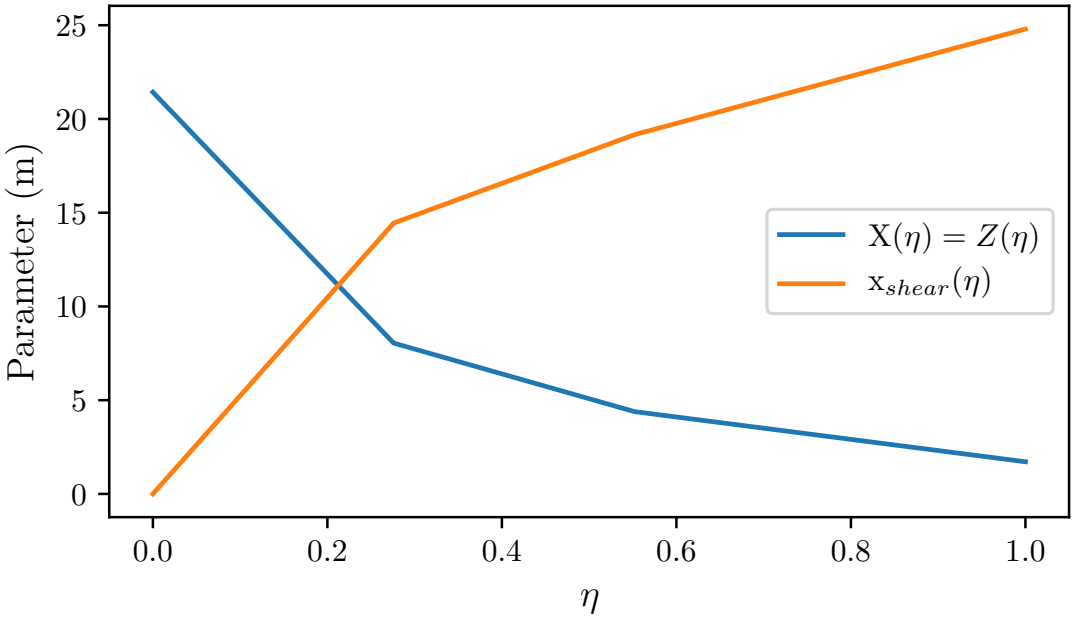

Fig. 3.7: Example of parameter variation with span.

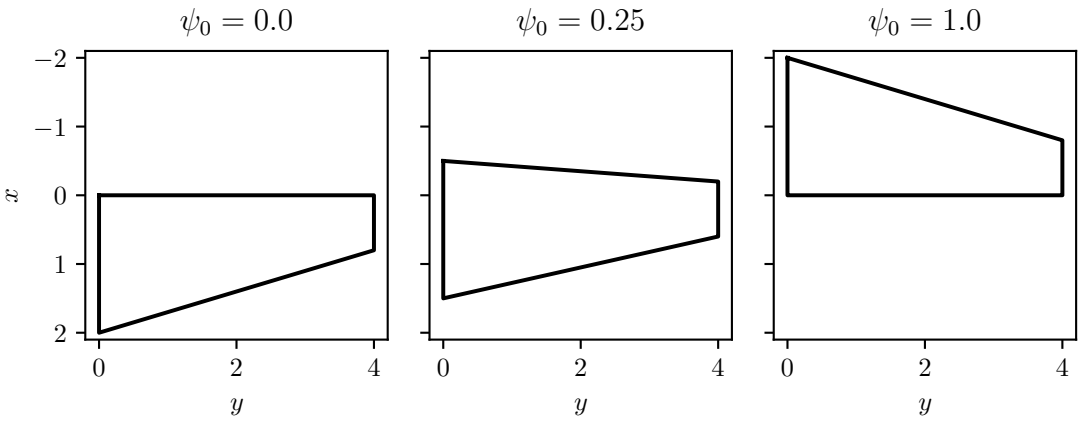

Fig. 3.8: Wing planform change with shift of reference coordinate system, 0 degrees sweep.

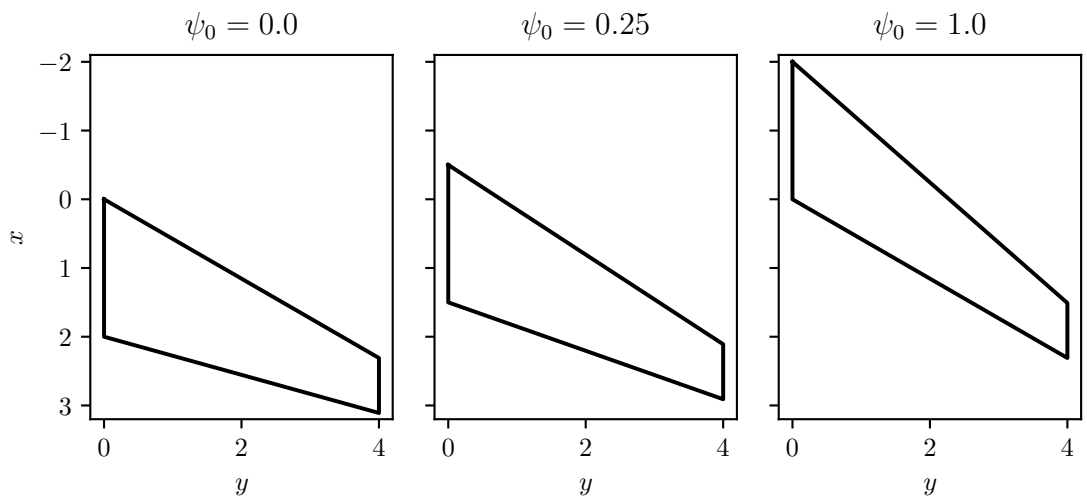

Fig. 3.9: Wing planform change with shift of reference coordinate system, 30 degrees sweep.

it via the $X(\eta)$ and $Z(\eta)$ parametric functions. If $X(\eta) = Z(\eta)$ and $\psi_0 = 0.5$, then the result will be an axisymmetric body. An example of a supersonic fuselage generated using three-dimensional CST equations is shown in Fig. 3.10. Class and shape functions can

Fig. 3.10: Example of fuselage surface generated using CST equations.

also be used for $X(\eta)$ and $Z(\eta)$. Taking this approach, Eq. 3.13 can be reduced to the axisymmetric equations introduced by Kulfan [78].

Equation 3.13 provides each surface in a local coordinate frame. To obtain the surface of a complete aircraft, the individual surfaces must be brought into a global coordinate frame and oriented appropriately. Euler angles or quaternions can be used to rotate each surface in the global frame and a position vector can be used for translation.

3.1.2 Surface Intersections

The panel method employed in this work requires a watertight description of the outer

mold line of the aircraft. This necessitates that the intersections between the individual CST surfaces that make up each component of the aircraft be known. Since the CST formulation provides an analytical equation for each surface, it was initially thought that a closed form solution could be found for these intersections. However, due to the non-linear nature of the CST equations, efforts to obtain a closed form solution were unsuccessful. However, a very simple and yet effective method was found based on fixed point iteration [80]. This section will outline the procedure for this method.

The intersection method essentially consists of guessing an initial point on one of the surfaces (surface 1) and then projecting that point onto the other surface (surface 2) along one of the axis of the global coordinate system. This yields a point on surface 2 that can be projected back onto surface 1 along a different axis of the global coordinate system. This process is repeated in an iterative fashion until convergence is achieved or the method diverges.

This process is best understood visually and with a specific example. An example of a simple wing and fuselage intersection as shown in Fig. 3.11 will be used. In this example, the subscripts w and f indicate values for the wing and fuselage respectively. For a given ψ_w and an initial guess of η_w, a point (x_0, y_0, z_0) on the surface of the wing can be calculated using the CST equation for the wing. Using the x_0 and z_0 coordinates and the inverse of Eq. 3.13, the ψ_f and η_f of the fuselage corresponding to x_0 and z_0 can be calculated. This information is then plugged into the fuselage CST equation to calculate y_1 on the surface of the fuselage. Using the inverse of the wing CST equation, a new η_w corresponding to y_1 is calculated. The given ψ_w and the new η_w are then used to repeat this same process over again. The process is iterated until the distance between the new point and the previous point falls between a specified tolerance.

Note that the method is not guaranteed to converge, and while good behavior is achieved in the simple cases explored in this work, the method is not robust to the general case of surfaces at arbitrary orientations to each other. Additionally, for the wing-fuselage case just demonstrated, the local coordinate systems of the wing and fuselage line up such

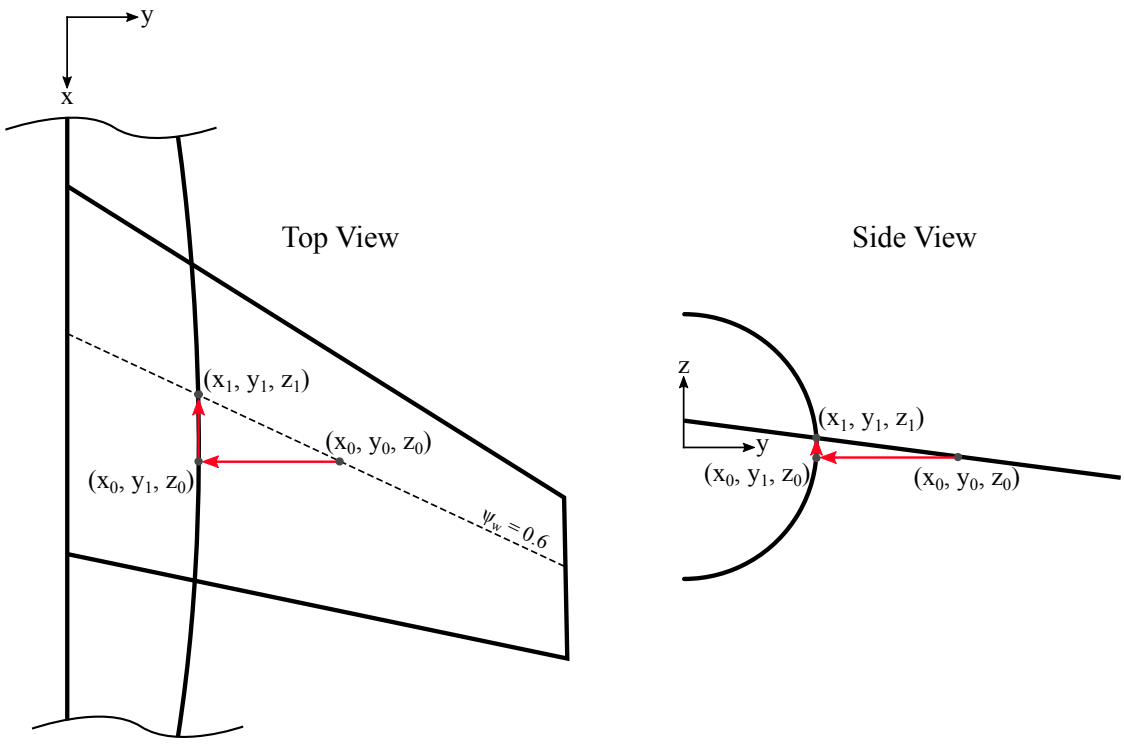

Fig. 3.11: Example of intersection method.

that only the inverse of x and y in Eq. 3.13 need to be computed. In this case, the inverse can be solved directly by first computing the inverse of y to obtain η and then using this to compute the inverse of x. In other possible orientations of the two coordinate systems, performing the necessary inverse calculations will require an iterative solution due to the non-linear nature of the equations.

The method outlined in this section is able to provide intersection information at discrete points corresponding to user specified stations in ψ or η of one of the surfaces. Ideally, a continuous description of each intersection could be obtained. Due to the discrete nature of the intersection solution, the geometry description and meshing are coupled. This coupling will be explained in detail in section 3.2.2 once more context has been provided for how the meshing is performed.

3.1.3 Reproducing Existing Geometries

The CST formulation has been shown to be flexible enough to accurately represent

a wide range of common aircraft geometries [78]. However, it is often not a straightforward task to back out the parameters that most accurately reproduce an existing three-dimensional configuration. This is due to the large number of parameters that need to be fit and the fact that each of these parameters do not have independent influences on the shape. Additionally, an appropriate metric for the error between two three-dimensional surfaces needs to be defined.

Leal, et al. [80] overcame these issues by separating the fitting process into two steps. First, all terms except for the class exponents and the shape coefficients are either specified from what is known about the geometry or curve fit. In the case of a wing, this would likely correspond to obtaining a curve fit for the leading edge of the wing ($\psi_0 = 0$) as well as the twist and chord distributions. In the second step, a fit of the class exponents and shape coefficients is performed utilizing the fits from the first step.

The second step requires a definition of an error metric between the CST surface and the data being fit. One approach is to use the average distance between each point on the surface being fit and the projection of each point onto the CST surface. In other words, ψ and η values for each data point are obtained using the inverse of Eq. 3.13 and then used to calculate the corresponding points on the CST surface. The error then becomes the distance between the data points and the corresponding points on the CST surface. This metric was used successfully in the work outlined by Leal et al. [80]. Another possible error metric is the Hausdorff distance also known as the Pompeiu-Hausdorff distance [81]. Since the Hausdorff distance is calculated using two discrete sets of points, the CST surface would need to be first evaluated at a grid of points over the surface.

Once the parameter values are fit, the CST equations provide a fully parameterized model of the geometry that can be used as initial conditions for shape optimization studies. However, since the CST equations are a curve fit there is inevitably some error between the CST equations and existing geometry being modeled. Studies of this error need to be performed in order to understand how the error in the geometric model is affecting the error in the aerodynamic results.

For the purpose of the performing these types of studies as well as performing benchmarks of the current framework, a more accurate representation of existing geometries is desired. In the current work, this was done using multivariate cubic interpolation to translate between the existing unstructured CFD surface grids and the structured grids required by PANAIR.

3.2 Nearfield Solution

The next step in the framework is to obtain a solution of the flow directly around the aircraft. The nearfield solution provides the aerodynamic forces and moments on the aircraft as well as the pressure signature required for sonic boom prediction. This section will outline the use of high-order panel codes to obtain this solution, including the governing equations being solved and the problem formulation.

3.2.1 The Prandtl-Glauert Equation

The PANAIR code solves the Prandtl-Glauert equation

$$(1 - M_\infty^2)\phi_{xx} + \phi_{yy} + \phi_{zz} = 0 \tag{3.15}$$

which provides a linearized description of steady, inviscid, irrotational, isentropic flow. The derivation of this equation can be found in several resources [82,83] and will not be addressed in detail here.

The ϕ term is a perturbation potential which is defined as the difference between the velocity potential Φ and the freestream potential Φ_∞

$$\phi = \Phi - \Phi_\infty \tag{3.16}$$

Thus, the velocity can be written as the sum of the freestream velocity $\overrightarrow{V_\infty}$ and the perturbation velocity $\overrightarrow{v}$

$$\overrightarrow{V} = \nabla\Phi = \nabla\Phi_\infty + \nabla\phi = \overrightarrow{V}_\infty + \overrightarrow{v} \tag{3.17}$$

In obtaining the Prandtl-Glauert equation, two primary assumptions were made [83]. These assumptions are

$$M_\infty^2 \, |\overrightarrow{v}| \ll 1 - M_\infty^2 \tag{3.18}$$

$$M_\infty^2 \, |\overrightarrow{v}| \ll 1 \tag{3.19}$$

Considering these two assumptions, it becomes apparent that the Prandtl-Glauert equation breaks down at large perturbation velocities and at Mach numbers near transonic or much greater than 1. The general rule of thumb, is that the linearized equation is valid for $0 \leq M_\infty \leq 0.8$ and $M_\infty \leq 5$ [82]. Additionally, the assumption of small perturbation velocities and isentropic flow (weak shocks only) limits the application to long thin geometries at small angles of attack. In practice, it is not always clear how well the assumptions hold until after a solution is realized and the resulting velocities can be inspected.

The Prandtl-Glauert equation can be rescaled to obtain a simpler form [83]. This is done with the coordinate rescalings

$$\overline{x} = x \tag{3.20}$$

$$\overline{y} = \beta y \tag{3.21}$$

$$\overline{z} = \beta z \tag{3.22}$$

where

$$\beta = \sqrt{s(1 - M_\infty^2)} \tag{3.23}$$

and

$$s = sign(1 - M_\infty^2) \tag{3.24}$$

The resulting rescaled equation is

$$s\phi_{\overline{x}\overline{x}} + \phi_{\overline{y}\overline{y}} + \phi_{\overline{z}\overline{z}} = 0 \tag{3.25}$$

It should be noted by comparing Eq. 3.15 and Eq. 3.25 that subsonic Mach numbers

result in an equivalent incompressible case and supersonic Mach numbers result in an equivalent $M = \sqrt{2}$ case. Although the rescaled equations for the subsonic and supersonic cases only differ by the sign on the first term, this results in completely different solutions and behavior. The subsonic case ($s = 1$) is called Laplace's equation and is elliptic in nature, meaning that information is propagated everywhere throughout the flow. On the other hand, the supersonic case ($s = -1$) is called the wave equation and is hyperbolic in nature, meaning that information is only propagated downstream inside the Mach cone.

In developing a panel solution, the Prandtl-Glauert equation is transformed into an integral form. For subsonic compressible flow, this is done using Green's theorems which relate a function that is harmonic and continuously differentiable on a bounded region to the potential distributions on the boundary [84]. An analogous integral equation can be obtained for supersonic flow by using supersonic source and doublet distributions and limiting the integral to its finite part [85]. The derivation of the supersonic integral equations and the corresponding boundary conditions used in PANAIR are are outlined in detail by Ehler et al. [52] and will not be repeated in this work.

For the present work, it is sufficient to understand the capabilities as well as the restrictions placed upon the solution by the formulation. As discussed in this section, solutions are limited to steady, inviscid, irrotational, isentropic supersonic flow about long slender geometries at low angles of attack. For these types of geometries, the assumptions of isentropic shocks and small perturbation velocities hold and the resulting solutions can provide accurate information about the non-viscous aerodynamic forces on the aircraft as well as a description of the flow immediately around the aircraft.

3.2.2 Problem Specification

In order to obtain a solution from PANAIR, surface meshes must be generating for the various surfaces of the aircraft and appropriate boundary conditions and wakes must be specified. All the necessary information for a given case is specified in the PANAIR input file. This section will outline the methods developed for generating the necessary surfaces meshes as well as the appropriate settings and boundary conditions.

One of the challenges in developing the proposed framework is automating the process of mesh generation from the parameterized geometry description. Instead of developing algorithms to handle arbitrary numbers of surfaces and orientations, the problem is much simplified if a given configuration of surfaces is assumed [10]. Thus, for the current work, tools were developed to allow the user to specify a specific configuration of surfaces which can then be meshed in an automated fashion. In other words, for a given configuration of surfaces, code must be written to handle the details of the orientations and intersections of the surfaces. Once this is done, the parameters controlling the shape of the surfaces can be changed and a surface mesh generated without any user input. Bounds should be placed on the parameters such that the changes in the surfaces don't violate the orientations and intersections of the surfaces assumed in the code generating the mesh.

The PANAIR solution requires that the boundary conditions, which includes surface and wake boundaries, be specified using what are called networks. Each network is made up of a structured grid of panels where each panels is defined by four corner points and no gaps exist between panels. Thus, to specify a network, the user provides a two-dimensional array of the corner points of the panels in the network. Network edges shared with other networks are called abutments. Along abutments between networks the points of each network must match within a tight tolerance. PANAIR does allow for mismatching of points along abutments but requires the user to input additional information on how to handle the mismatch. If all of the points along abutments match, PANAIR is able to recognize and specify the appropriate relationships between networks for the solution. For the current work, the meshing is handled in such a way that the points will always match along network boundaries. It is also important to note that many of the common boundary conditions used by PANAIR assume that the networks that make up the surface of the geometry form a watertight surface, completely separating the solution inside the geometry from the solution outside. The exception to this is along planes of symmetry where no networks need to be specified to close off the geometry.

In order to obtain the PANAIR networks from the CST surfaces, a relationship was

defined between a network and a CST surface. In this work, a network corresponds to a region of a CST surface defined by a closed loop of four curves in the CST parameter space. Thus, a single CST surface may define multiple networks but a network may never be comprised of more than one CST surface.

Figure 3.12 shows an example parameter space with a region corresponding to a network. The curves defining the network boundaries must be single-valued in the direction they correspond to. The two curves on the sides define the upper and lower boundaries in ψ and must be single-valued in η. The two curves on the top and bottom define the upper and lower boundaries in η and must be single valued in ψ. With the region corresponding to a network defined by four curves in this manner, it becomes easy to define a structured grid over the network.

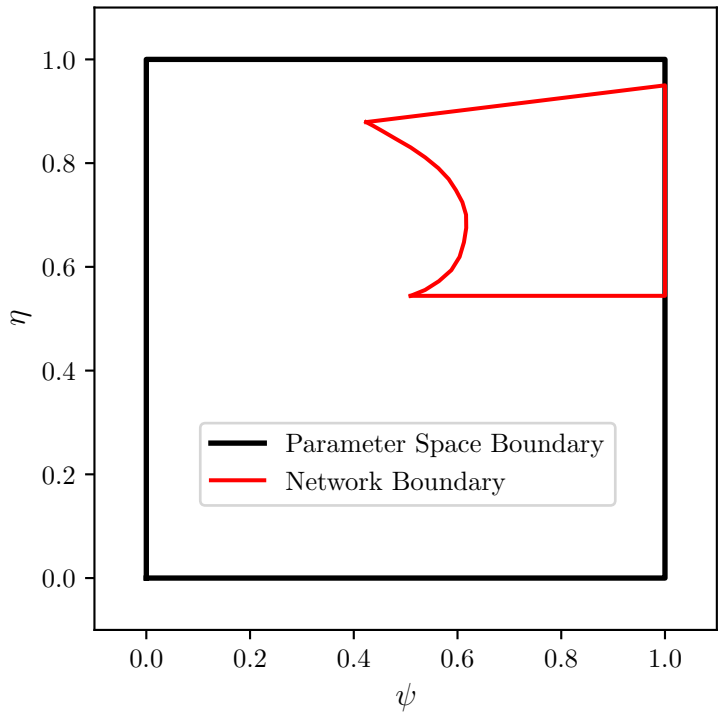

Fig. 3.12: Example network boundary in the parameter space.

An example of the parameter spaces, network boundaries, and corresponding grids for

a wing fuselage configuration is shown in Fig. 3.13. The fuselage is represented with a single CST surface and two networks. The upper and lower surfaces of the wing are each represented with a CST surface and three networks. Only the wing upper surface is shown in Fig. 3.13. Both linear and cosine spaced points have been used between network boundaries to redistribute points as desired. Notice how an empty region has been cut out in the center of the fuselage parameter space by the wing and the root of the wing has been cut off where it intersects the fuselage.

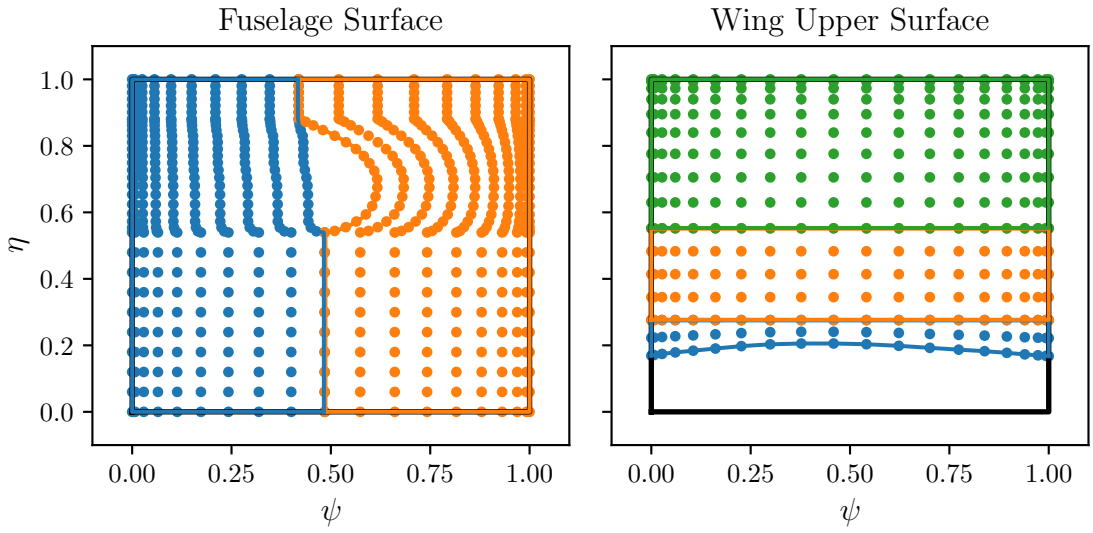

Fig. 3.13: Example networks and grids for a wing-fuselage configuration. Colors used to distinguish separate networks.

With the requirement of points matching along network abutments, the meshing of a given network is often dependant on the mesh used in adjacent networks. Additionally, since the intersection algorithm used yields discrete points, the meshing and intersection processes are usually done at the same time. A good example of how this situation might be handled is illustrated with the wing-fuselage configuration shown in Fig. 3.13. First, points at the intersection between the upper surface of the wing and the fuselage are found that correspond to the number of points and spacing desired along the chord of the wing. This process is also done for the lower surface of the wing. The inverse of the CST functions

for the wing and fuselage surfaces are then used to find the corresponding ψ and η values of these points in the wing and fuselage parameter spaces. These intersection points are used along with additional information from the user to define four sets of points for the four boundaries of each network. These boundaries are then used to generate the grids for each network in ψ and η. These grids are then plugged into the CST functions to obtain the x, y, z point grids for each network.

Each network has an outer and inner surface. Which side is which depends on the ordering of the network points as they are passed to PANAIR. The specific details of this ordering is outlined in the PANAIR user manual [86].

PANAIR allows for the details of the boundary conditions to be specified by the user but also provides the most common boundary conditions via network types. As recommended by the user manual, the type 11 network which implements velocity impermeability on a thick surface was used for all surfaces sub-inclined to the freestream Mach number. The type 5 boundary condition was used for super-inclined surfaces such as on the tail cap of the fuselage. The standard type 18 wake was used for all wakes except for the wake connecting the wing and fuselage wakes for which a type 20 wake was used.

A detailed example of the networks, wakes, and corresponding paneling of a wing-fuselage configuration can be found in Chapter 5.

3.3 Propagation and Noise Metrics

Once a solution of the nearfield flow is obtained, the nearfield signature is passed into a propagation code which propagates the signature down to the ground. The ground signature is then passed into a noise metrics code which outputs a loudness.

The nearfield signature is the deviation in the local pressure from the freestream pressure measured along a line sensor that runs parallel to the freestream at some distance away from the aircraft. PANAIR allows for off-body points to be specified in the input file and will output the flow properties at these points along with the rest of the solution. This functionality was used to measure the pressure coefficient along the line sensor. The number of samples along this line sensor was limited to roughly 1600 due to hard-coded

limits in PANAIR. The pressure coefficient can be converted to the standard representation using

$$\frac{P - P_\infty}{P_\infty} = \frac{1}{2}\gamma M^2 C_p \tag{3.26}$$

In this work, the NASA developed sBOOM code [43] was used to propagate the nearfield signature down to the ground. It was found that the use of 40,000 propagation points and 8,000 padding points provided a converged solution in sBOOM and this was used in most cases. The standard atmosphere built into sBOOM was used for all the results presented in this work.

Once the pressure signature at the ground is obtained, Stevens' Mark VII method [66] is then used to calculate the perceived loudness. To do this, a Fast Fourier Transform (FFT) is used to convert the signal to the frequency domain. The energy contained in each third-octave band and the corresponding loudness is then calculated. Stevens' method provides weightings for the loudness in each band that allows for the calculation of a perceived loudness in decibels (PLdB). This method takes into account the sensitivities of the human ear in order to determine a loudness based on human perception. A code developed at Utah State University, called PyLdB, that implements this method is used in the current work [75].

CHAPTER 4

VERIFICATION AND BENCHMARK OF AXISYMMETRIC GEOMETRY

The axisymmetric geometry provided in the 2017 AIAA Sonic Boom Prediction Workshop provides a simple starting point to begin investigating the performance of the present framework. The investigation of this geometry will focus first on verifying that a correct solution is being obtained and then on benchmarking the solution against high-fidelity results.

4.1 Solution Verification

The verification focuses on two primary areas. First, an investigation is performed into how the grid used in the nearfield solution affects the resulting loudness prediction. Second, an investigation is performed into the effect of the distance between the aircraft and the location at which the nearfield signature is measured on the perceived loudness prediction. The results of these investigations provide insight into the grid refinement necessary to achieve the appropriate balance between accuracy and run time and insight into the effect of the linear nearfield solution on the loudness prediction.

4.1.1 Grid Convergence Study

In the current framework, there are multiple tools and communication points that use discrete data. To effectively use these tools, it is important to understand the effects of the coarseness of the discretizations on the solution. Once these effects are understood, it is easier for the user to ensure that the best solution accuracy is being obtained with the time and computational resources available. The main discretization evaluated in this work is the number of panels used to describe the geometry in the aerodynamic model.

The PANAIR program requires that the case geometry be described by a structured surface mesh where each cell represents a panel. In the axisymmetric case, the PANAIR

surface mesh has two primary components: the mesh spacing along the centerline or axial direction and the mesh spacing around the circumference of the body or tangential direction as seen in Fig. 4.1. Because the PANAIR code was developed in the 70s and 80s, limits on the file sizes are hard coded. With the version of PANAIR used in the current work, cases above 7500 to 8000 panels fail with an error. Efforts to remove or change these limits have thus far been unsuccessful. Due to these limits, the current work will investigate the axial and tangential spacing separately, allowing for greater refinement to be achieved along the direction of interest for each case.

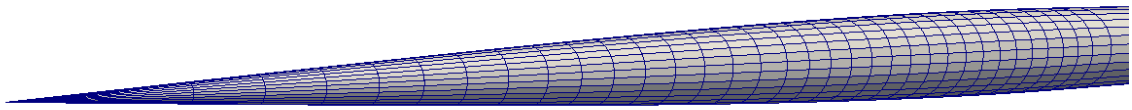

Fig. 4.1: Example structured mesh of AXIE geometry.

The AXIE geometry is available from NASA as a series of points that represent the radius as a function of distance down the centerline. A simple coarsening algorithm is developed to remove unnecessary points in the axial direction based on how much each point contributes to the geometry description. This coarsening algorithm is used on the original AXIE geometry description to obtain a coarse, medium, and fine representation with 187, 375, and 751 points respectively in the axial direction. These representations are used to create surface meshes which are passed to the sonic boom prediction framework to obtain nearfield pressure signatures, ground signatures, and corresponding perceived loudness levels at the same flight conditions used in the Sonic Boom Prediction Workshop. These conditions consist of an altitude of 15760 m in the U.S. Standard Atmosphere (1976) [87] and a flight Mach number of 1.6. The nearfield signatures for the grid convergence study are all taken at one body length away from the aircraft, where one body length is 32.92 m as specified by the workshop. Figures 4.2 and 4.3 compare the nearfield and ground signatures respectively for the different grid refinements.

Table 4.1: Loudness at the ground vs. axial refinement.

Mesh	Number of Panels		Loudness		
	Axial	Tangential	PLdB	A-Weighted	C-Weighted
Coarse	186	36	77.62	63.06	90.32
Medium	374	36	77.57	63.09	90.33
Fine	750	36	77.59	63.10	90.34

All three levels of mesh refinement produce similar nearfield signatures, as shown in Fig. 4.2 . While the overall signature shapes are similar, the coarser grids produce signals with more small-scale noise. This is likely because the coarser grids have sharp corners which produce small shocks when the nearfield solution is obtained from PANAIR.

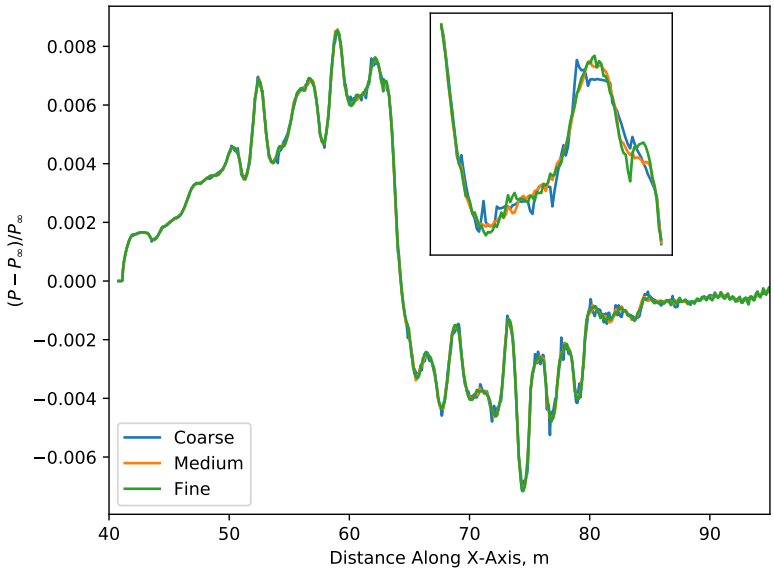

Fig. 4.2: Nearfield signatures vs. axial refinement.

After being propagated through the atmosphere, the ground signatures are almost indistinguishable as observed in Fig. 4.3. It appears that the small scale shocks produced by the coarser grids are smoothed out and effectively disappear as the signal is propagated down to the ground. This is further seen in the predicted perceived loudness at the ground, as shown in Table 4.1, where little variation is seen in the predicted loudness even for the coarsest mesh.

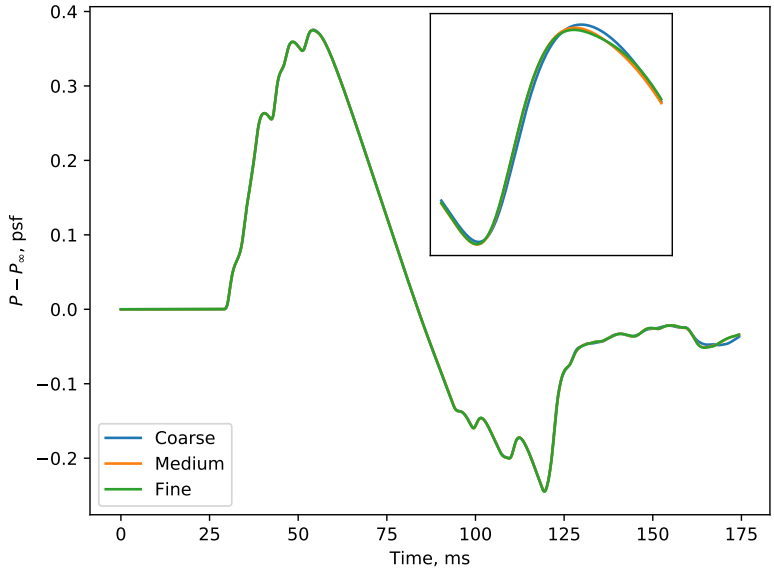

Fig. 4.3: Ground signatures vs. axial refinement.

The effect of the tangential refinement is also investigated in a similar manner. The medium level of axial refinement, 374 panels in the axial direction, is used along with three levels of refinement for the tangential direction. Because PANAIR is able to take advantage of symmetry in the problem, the geometry only needs to be revolved a quarter of a full revolution. The coarse, medium, and fine grids for the tangential study have 5, 10, and 20 points respectively in the tangential direction, corresponding to 16, 36, and 76 panels around the full circumference.

Figures 4.4 and 4.5 show the nearfield and ground signature respectively for the varying levels of mesh refinement in the tangential direction. The coarse mesh is clearly insufficient and produces large oscillations at the tail end of the nearfield signature that also appear in the ground signature. However, the differences seen between the medium and fine meshes appear to be small.

The corresponding loudness levels for the tangential grid refinement study are shown in Table 4.2. A finer mesh in the tangential direction better resolves the cross-sectional area and results in slightly larger peaks in the pressure signature and an increase in the calculated perceived loudness.

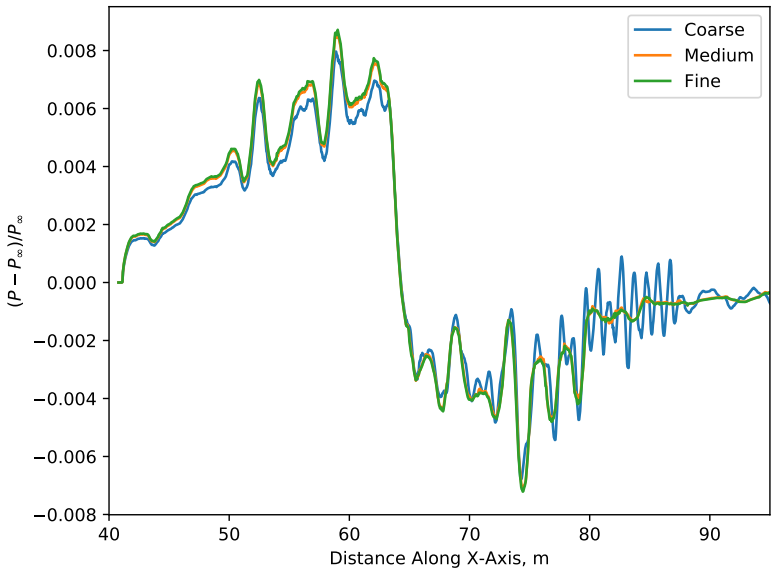

Fig. 4.4: Nearfield signatures vs. tangential refinement.

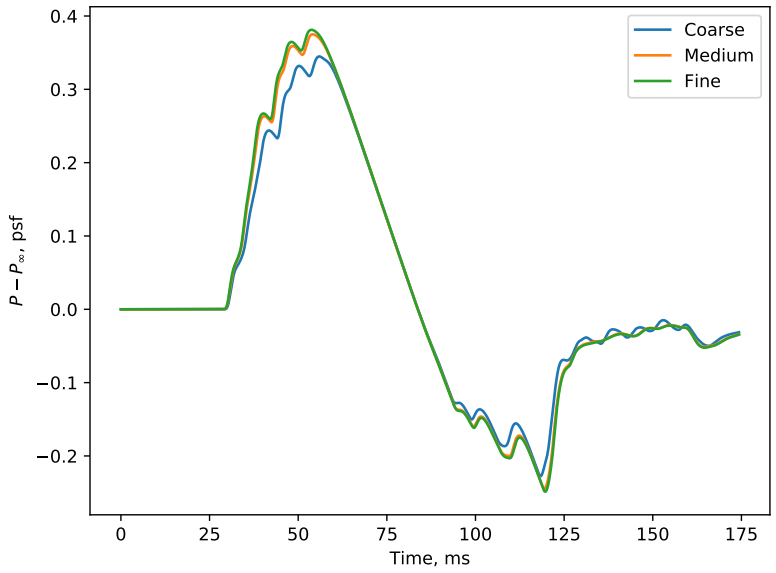

Fig. 4.5: Ground signatures vs. tangential refinement.

4.1.2 Sensor Location Study

The second part of the axisymmetric validation is to investigate the effect of the nearfield sensor location on the predicted nearfield signature, ground signature, and corresponding loudness. There are two effects that the sensor location has on the sonic boom

Table 4.2: Loudness at the ground vs. tangential refinement.

Mesh	Number of Panels		Loudness		
	Axial	Tangential	PLdB	A-Weighted	C-Weighted
Coarse	375	16	77.17	63.06	89.63
Medium	375	36	77.57	63.09	90.33
Fine	375	76	77.78	63.28	90.49

pressure signature. First, the nearfield pressure signature is better approximated as a line source the further it is taken away from the body. This is important because the propagation code assumes that this is the case. Second, there is a non-linear steepening or "aging" of the pressure signature as it travels away from the body. PANAIR provides a linearized solution of the flow field and is unable to account for the nonlinearity. Thus, the further the nearfield signature is taken away from the body, the more time the linear and non-linear solutions have had a chance to diverge. Hereafter, this second type of error will be called non-linear error.

To investigate the effect of the sensor location, four sensor locations where used at one, three, five, and ten body lengths away from the aircraft. The same flight conditions used in the grid convergence study were used here along with a mesh containing 500 axial by 56 tangential panels. The nearfield signatures obtained at the different sensor locations can be easily compared by scaling them by $\sqrt{R/L}$ to account for the effects of the natural pressure decay as shown in Fig. 4.6. There is a significant difference between the signatures at one and three body lengths but this difference diminishes at further distances. However, the same is not true for the ground signature.

The further away the nearfield signature is taken from the body, the greater the distance of propagation over which the effects of nonlinearity are not properly accounted for. This is seen in Fig. 4.7 which shows the ground signatures corresponding to each nearfield signature in Fig. 4.6. Even though the nearfield signatures converge at distances far enough away from the body, the corresponding ground signatures continue to diverge. The resulting loudness values are shown in Table 4.3. The differences seen in the ground signature due to nearfield sensor location aren't as obvious in the corresponding perceived loudness. This is

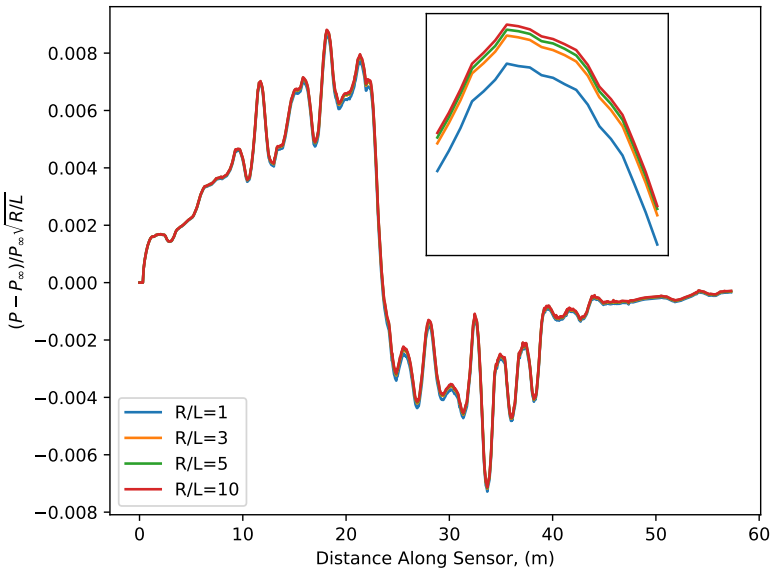

Fig. 4.6: Nearfield signatures vs. sensor location.

likely because the longer rise time and higher amplitude seen in the "under-aged" signatures tend to change the perceived loudness in opposing ways, which results in a small difference overall.

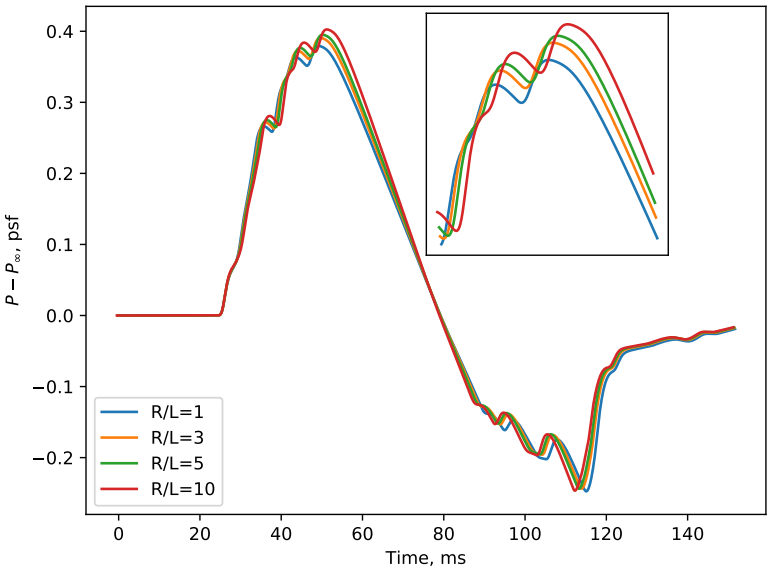

Fig. 4.7: Ground signatures vs. sensor location.

Table 4.3: Loudness at the ground vs. sensor location.

R/L	Number of Panels		Loudness		
	Axial	Tangential	PLdB	A-Weighted	C-Weighted
1	500	56	77.57	63.20	90.39
3	500	56	77.50	63.08	90.49
5	500	56	77.47	63.12	90.54
10	500	56	77.46	63.34	90.66

To mitigate the error due to the linearity of PANAIR at large sensor distances, one could potentially scale a signature taken at a far distance back up to a distance near the aircraft as done to generate Fig. 4.6. This scaled signature could then be propagated from this new closer location, reducing the distance over which the nonlinearity is not accounted for. An approach similar to this was taken by Chan [9] and resulted in a closer matching of Euler and experimental data.

4.2 Benchmarking Study

Results for the axisymmetric geometry are benchmarked in this section against high-fidelity results available from the AIAA Sonic Boom Prediction Workshop as well as collaborators from Texas A&M University. Specific results were selected for comparison in the current work because they had been submitted to the workshop by collaborators on the grant funding the current work. These include full Euler solutions generated by the CART3D and FUN3D codes. Collaborators at Texas A&M used their in-house UNS3D code [88] to provide a full Euler solution as well. In all cases, the flight conditions specified by the workshop were used along with a sensor distance of 5 body lengths. A PANAIR mesh of 360 axial by 76 tangential panels was chosen based on the results of the grid convergence studies. The number of propagation and padding points used in sBOOM for each case were 40,000 and 8,000 respectively.

The nearfield signatures for each code are shown in Fig. 4.8. It can be seen that the Euler solutions all lie roughly on top of each other. Although the PANAIR solution is shifted slightly from the Euler Solutions, it has a very similar shape. This shift in the PANAIR results is due to the linear assumptions built into the panel method. Essentially,

the non-linear aging of the signature has been neglected in the first five body lengths of the propagation. The effect of the linearity of PANAIR can also be seen in the signatures on the ground signatures as shown in Fig. 4.9. As in the nearfield signatures, it can be seen that, although under-aged, the PANAIR pressure signature at the ground matches the Euler solutions well.

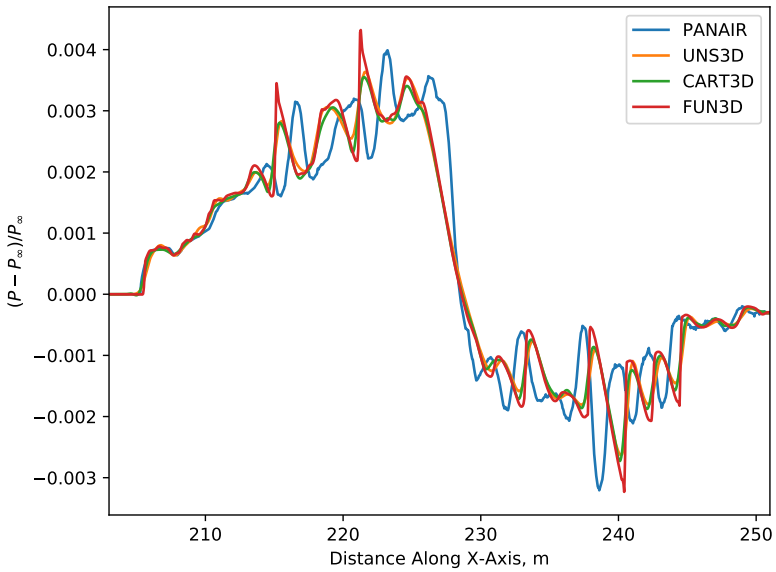

Fig. 4.8: Comparison of nearfield pressure signatures.

The perceived loudness predicted for each of these cases is shown in Fig. 4.10 along with the workshop mean and corresponding standard deviation. The workshop mean was generated using the finest grid solution of each Euler case submitted to the workshop. For consistency, the nearfield signatures of each case were propagated through sBOOM with the same settings and a perceived loudness calculated using PyLdB instead of using the workshop calculated loudness values.

The results of this benchmark show that PANAIR compares reasonably well to the high-fidelity Euler solutions for the AXIE geometry. This isn't totally unexpected since the AXIE geometry fits well in the assumptions of linearized supersonic flow. It should be noted that many of the grids for the workshop cases were over 12,000,000 cells.

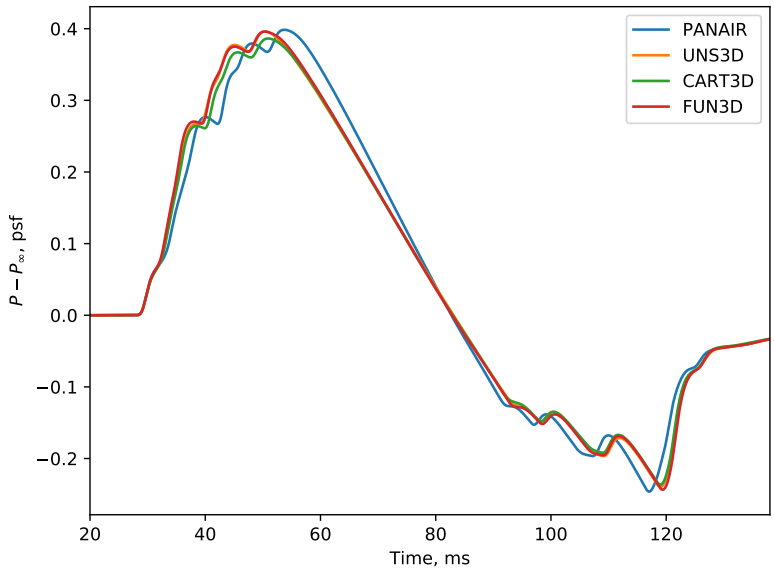

Fig. 4.9: Comparison of ground pressure signatures.

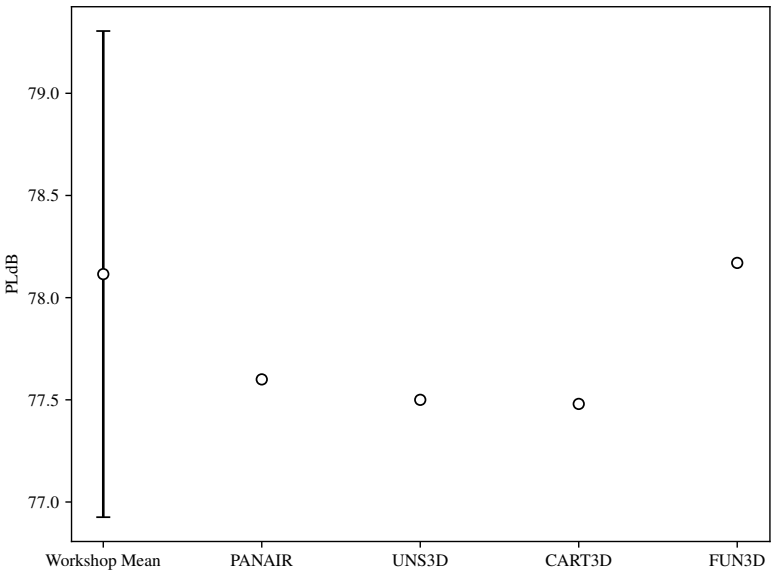

Fig. 4.10: Comparison of perceived loudness levels.

4.3 Summary of Axisymmetric Results

Solution convergence for an axisymmetric geometry was verified with grid convergence studies. Additionally, a study into the effect of nearfield sensor distance provided insight into the effect of the linearized panel solution. The panel solution allows a nearfield signature

to be taken at any distance away from the aircraft without additional cost. However, the further the nearfield signature is taken away from the body, the greater the error due to linearity of the PANAIR solution. Techniques similar to those used by Chan [9] could be used to overcome this error.

The nearfield and ground signatures and the perceived loudness levels were compared with high fidelity Euler solutions from collaborators and from the 2017 2nd AIAA Sonic Boom Prediction Workshop. The linearized solution of the panel method tended to produce an under-aged solution that was, otherwise, similar in shape to the high-fidelity solutions. The resulting perceived loudness levels compared well with the high-fidelity solutions.

The good agreement seen between the panel method and the high-fidelity Euler solutions is encouraging but by no means conclusive. In order to be an effective tool for low-boom design and optimization, PANAIR must also perform well for more complex geometries that include lifting and tail surfaces and even nacelles.

CHAPTER 5

VERIFICATION AND RESULTS OF WING-BODY GEOMETRY

The JAXA wing-body (JWB) geometry from the 2017 AIAA Sonic Boom Prediction workshop [53] is an ideal beginning case for verifying and understanding the panel solution for a lifting configuration. The geometry introduces several of the primary components of a full configuration without being overly complex. These components include fuselage and main wing geometries and the aspects of lift and asymmetry. If these fundamental components can not be appropriately modeled, there is no point laboring on the details of a full configuration. Once the solution is verified with this simpler geometry, one can confidently approach the remaining components found in a full configuration.

Before pursuing the details of the verification and benchmarking of the JWB geometry, it is helpful to view some of the preliminary results that were obtained with an initial set up of the case. Figure 5.1 compares the JWB nearfield signature obtained with PANAIR to that of a full Euler solution. It is seen that the PANAIR solution performs well with respect to what might be expected of a panel solution until the end of the signature. At the end of the signature, large spikes in the pressure occur that do not exist in the Euler solution. Even though the front portion of the signature matches the Euler solution reasonably well, the large spikes at the end result in large differences in the ground signature and the loudness.

Since similar spikes were not seen in the results of Chan [9], it was expected that some incorrect setting or boundary condition in PANAIR was the cause of the issue. Significant effort was expended digging into the user manuals and literature and testing different possible settings. However, nothing that was tried fixed the issue. Refining the grid only served to increase the spikes. At this point, efforts turned to seeking a deeper understanding of the fundamental formulation of PANAIR as well as seeking out people with substantial experience using the tool. Feedback from Matthew F. Smith (Boeing) and Stephen C. Smith (retiree of NASA Ames) who have both used PANAIR extensively in their professional

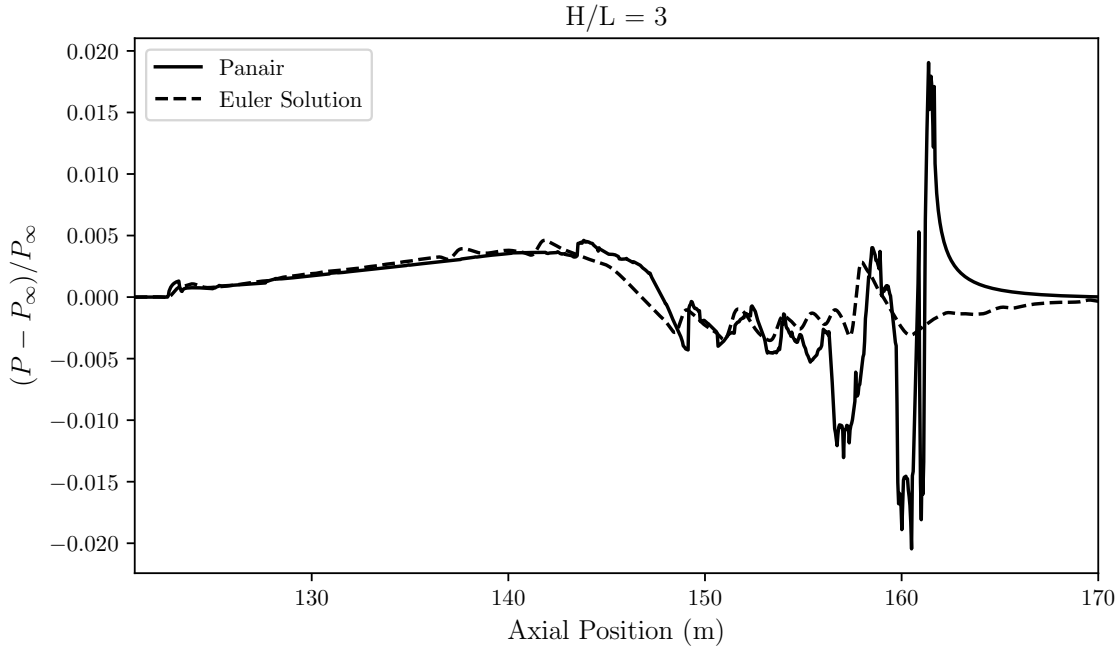

Fig. 5.1: Preliminary nearfield signature results for JAXA wing-body geometry.

careers helped verify that we were indeed setting up the cases correctly.

A quote from the paper that outlines the theory for PANAIR also yields insight into the problem [52].

> "In exact theory, the expansion waves are in the form of a continuous centered fan of characteristics instead of a single discontinuity. The approximation of expansion waves by an expansion shock is valid near the surface but is a poor representation of the flow at greater distances away from the surface. Linearized theory solutions involving rapid expansions can be expected to yield good pressure distributions on the surface but the induced flow at large distances from the expansion surface will not be accurately described."

This quote establishes that, in the presence of strong expansions, good results are expected to be achieved in the surface pressure solution but not necessarily at large distances. Consequently, the verification of the solution should start by looking at the surface pressures and not the pressure away from the body. Additionally, verifying the solution from the integrated result of the nearfield signature provides scant insight into the location or

cause of the issues. Once it is clear that a good surface pressure solution can be obtained, then the accuracy of the off-body solution can be investigated.

A preliminary comparison of the surface pressures produced by the PANAIR solution and an Euler solution is shown in Fig. 5.2 and 5.3 where the top half of the geometry is showing PANAIR results and the bottom half Euler results. The Euler solution was obtained using the UNS3D code developed at Texas A&M [88]. The solution of the nose of the aircraft was not included in the figures because it matched very well. For the aft end of the geometry, it can be seen that, qualitatively, the surface solution matches remarkably well except for regions at the outboard portion of the wing and at the tail of the fuselage.

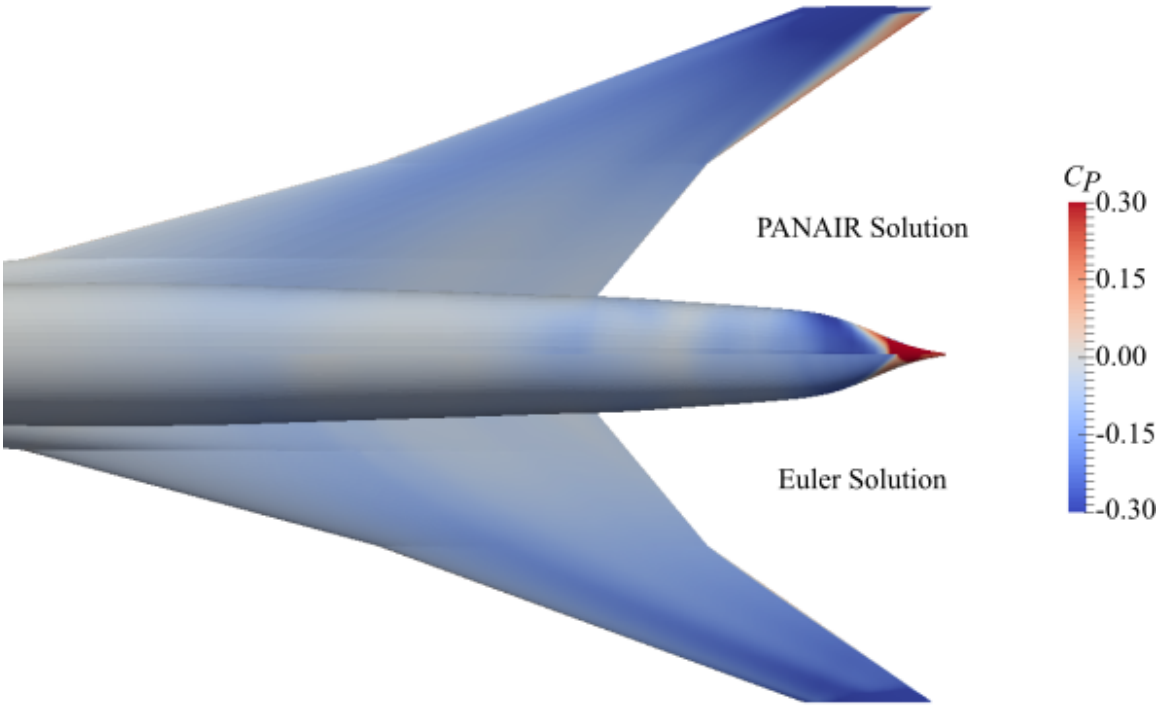

Fig. 5.2: Preliminary Comparison of PANAIR and Euler surface pressures for top surface of JAXA wing-body geometry.

This chapter focuses on verifying and improving the surface solution in the outboard and tip region of the wing and the tail of the fuselage. Due to the relative orientation

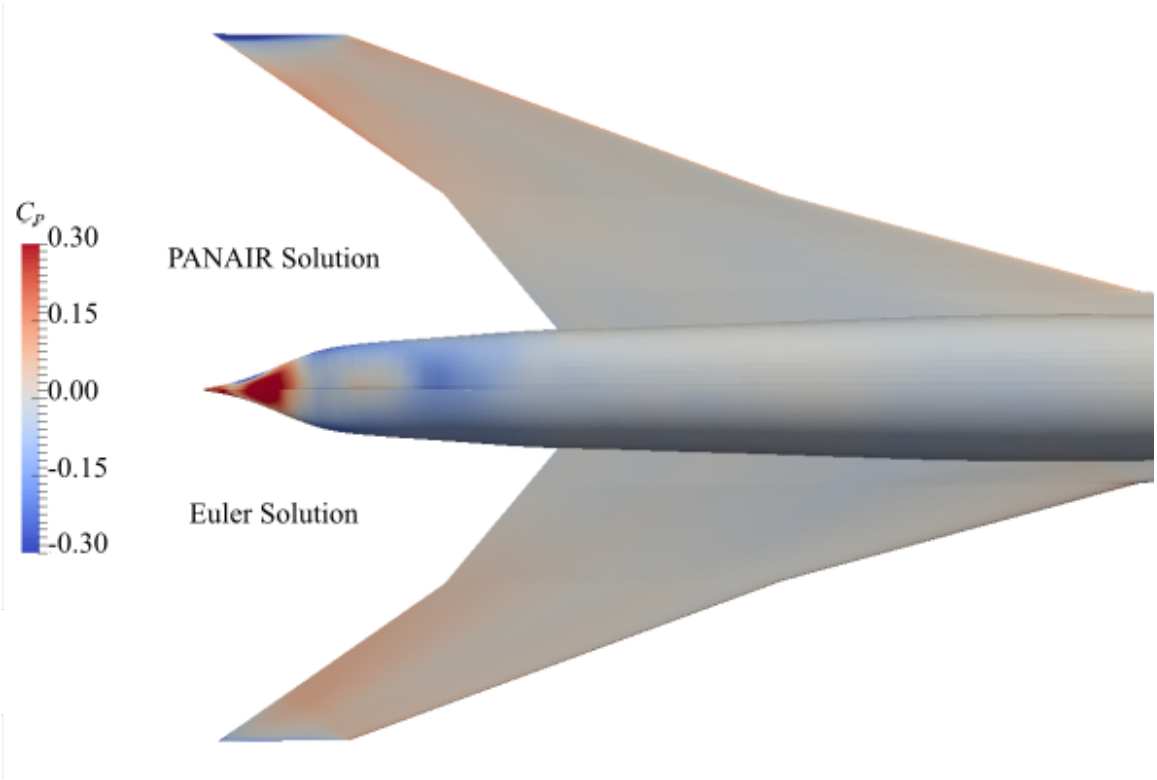

Fig. 5.3: Preliminary Comparison of PANAIR and Euler surface pressures for bottom surface of JAXA wing-body geometry.

of these regions and the flight Mach number, the surface solutions of the wing and the tail are mostly independent. Examining these regions separately allows for increased mesh refinement in the area of interest. After these regions are investigated, an examination of the off-body solution is performed.

5.1 General Description of Case Setup

Setting up a case for a wing-fuselage geometry in PANAIR includes providing appropriate surface and wake networks as well as specifying boundary conditions and various other settings.

Figure 5.4 provides a quick snapshot of the network meshes and the corresponding boundary conditions that were used in the present work. The type 11 network is the standard supersonic boundary condition and enforces velocity impermeability on the surface. A type 5 network was used on the tail cap for a superinclined surface boundary condition. The standard type 18 wake network was used for the wing with the default option of matchw=0. A type 20 wake network that maintains a constant doublet strength was used to connect the wing wake to the fuselage side and wake. Type 18 wakes with a matchw option of 1 were used on the fuselage as recommended in the user manual. However, no significant difference was noticed in the solution when the matchw=0 option was employed. An x-z symmetry plane was used such that only half of the geometry needed to be input.

5.2 Wing Study

A study of the wing is conducted in two portions. First, the validity of the solution is checked by examining the flow properties of the solution on the surface. Second, a grid convergence study is performed to further verify the solution and to understand the amount of paneling necessary to obtain a converged solution.

5.2.1 Solution Check

The validity of the panel solution for a given geometry can be easily checked by looking at several different aspects of the solution. For a good solution, the local mach numbers on

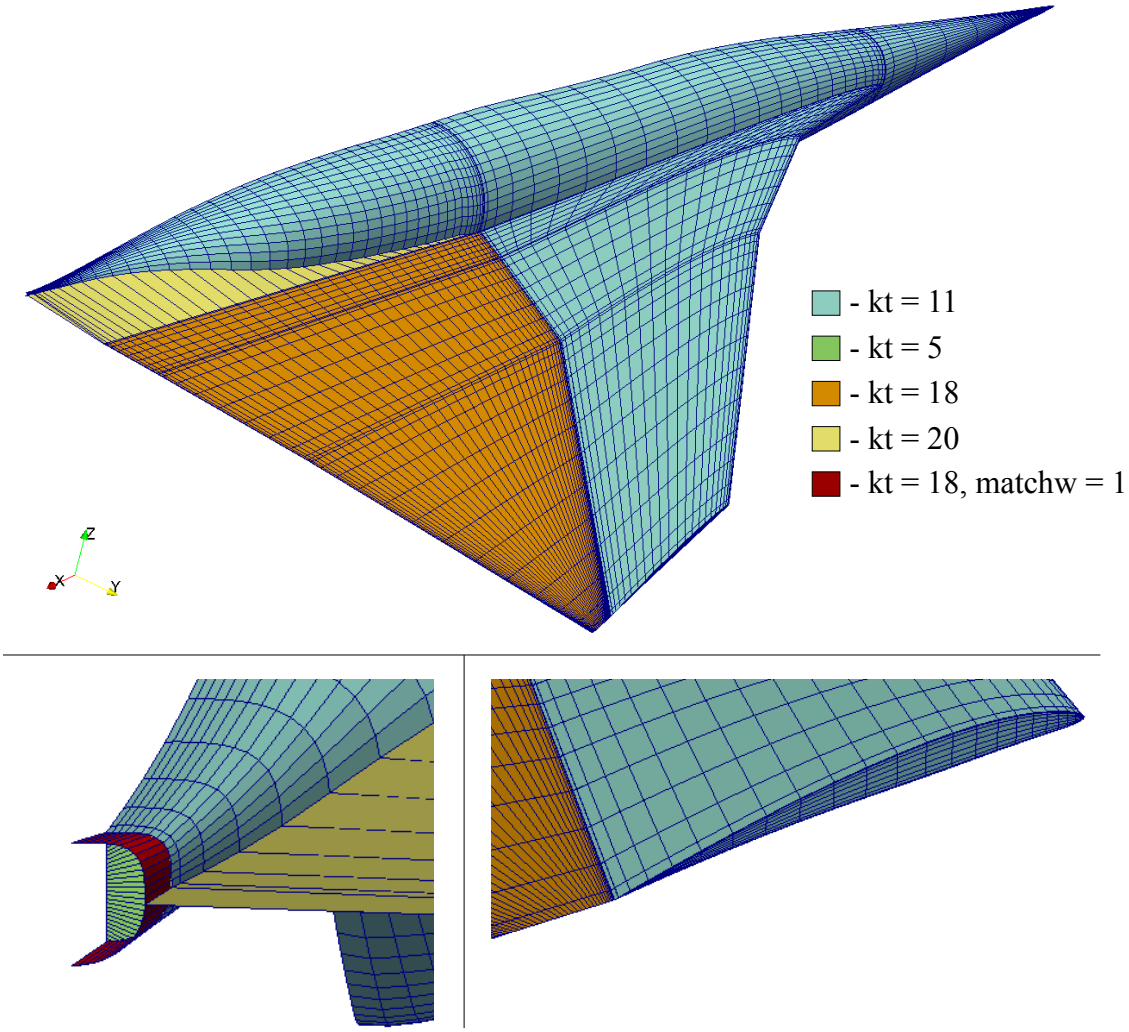

Fig. 5.4: Networks and boundary conditions for JWB geometry.

the surface should not be much larger than one and the mass flux normal to the surface should be close to zero.

An inspection of the Mach numbers on the surface of the wing reveal good results other than at the wing tip as shown in Fig. 5.5. These large and very unrealistic spikes in the Mach number at the wing tip are due to the sharp corners present there. These spikes are typical in a potential flow solution which predicts an infinite velocity around sharp corners. While large, these spikes are found only in small regions right at the wing tip and consequently don't have a large effect on the rest of the solution. Additionally, it will be shown in the following section that the area of the solution with these large spikes can be reduced by adding mesh resolution to the affected area.

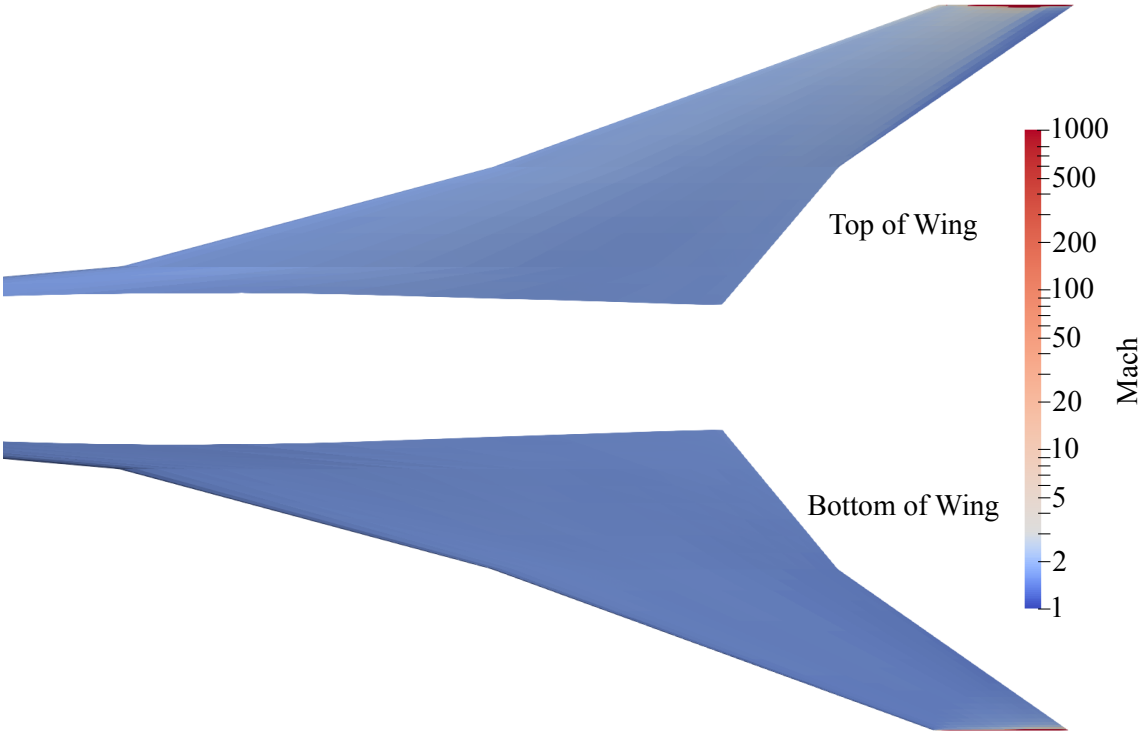

Fig. 5.5: Mach on top and bottom surfaces of wing.

For a wing with a symmetric airfoil at zero angle of attack, these large spikes in the Mach number at the wing tip disappear. In this case, no lift is being generated and there is

no cross-wise flow going around the sharp corners. Most cases of interest, however, will be producing lift, resulting in spikes in the Mach number at the wing tip. While not attempted in the current work, it is expected that rounded corners at the wing tip with sufficient surface mesh resolution would further mitigate the large spikes in the Mach number.

Another check on the solution is to look at the mass flux normal to the surface which for a perfect solution would be zero. Figure 5.6 shows the magnitude of the mass flux normal to the surface on the upper and lower surfaces of the wing. It can be seen that results over the wing are reasonable except except in small regions at the leading and trailing edges near the wing tip.

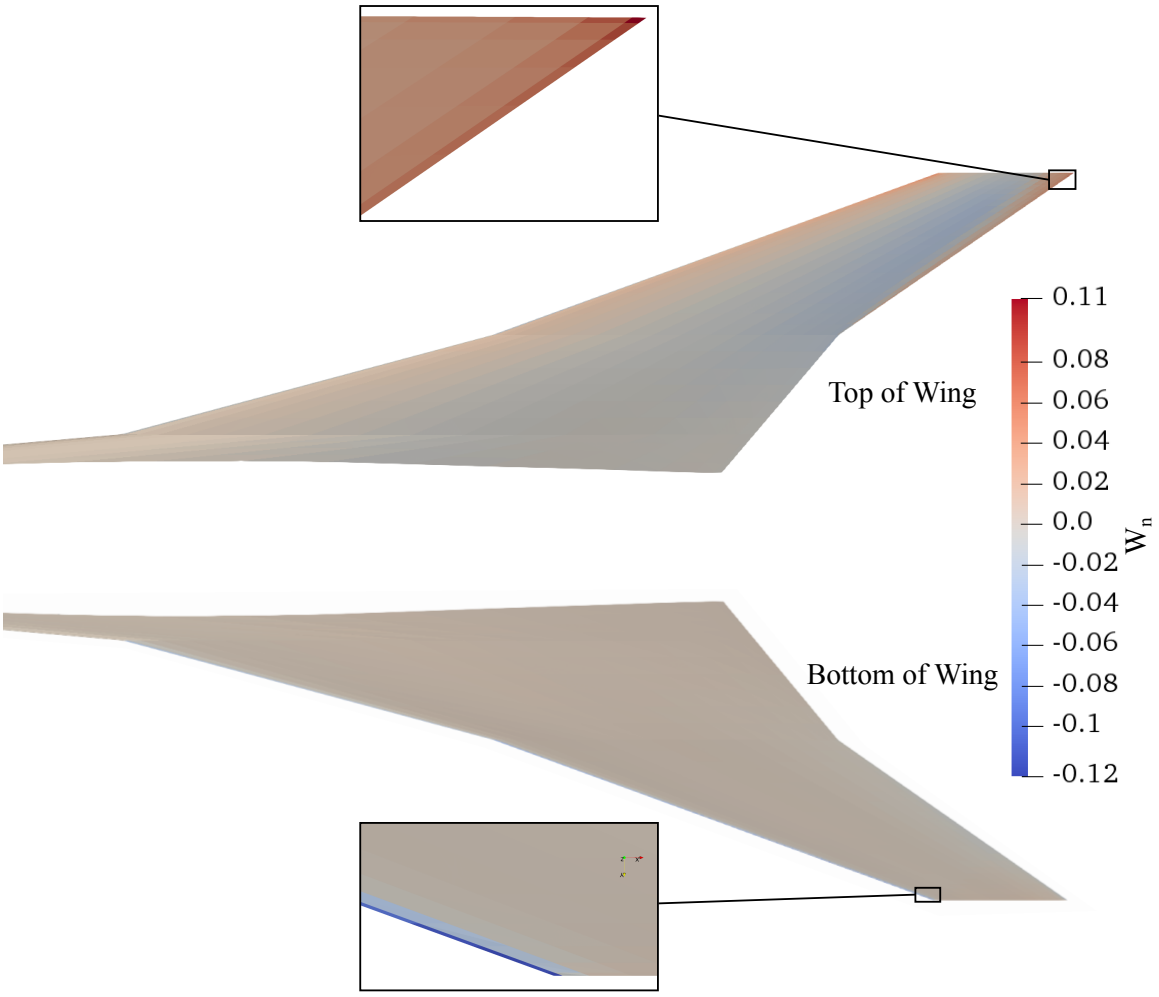

Fig. 5.6: Mass flux normal to surface on top and bottom of wing.

5.2.2 Grid Convergence Study

The grid convergence study for the wing is done in two portions. The first takes a qualitative look at how the grid resolution affects the low pressure region at the wing tip and also the shock across the trailing edge of the outboard portion of the wing. The convergence will then be examined in greater detail by looking at the surface pressures along two-dimensional chord-wise slices of the wing.

Based on the preliminary comparisons with the Euler solution and the results of the solution check, it seems that the greatest area of concern on the wing is the outboard portion. A basic understanding of how the grid resolution affects the surface pressure can be obtained by simply looking at contours of the surface pressure as the grid is refined. The grid refinement along the span of the wing and along the chord of the wing were examined separately to see the effects of each. Figure 5.7 shows three levels of grid refinement along the span with the chord-wise refinement held constant. It can be seen that the size of the low-pressure region at the wing tip is directly proportional to the panel width at the tip. These results are encouraging because it shows that the large and unrealistic spikes predicted by the potential flow solution at the sharp corners of the wing tip can be constrained to a small area of the solution.

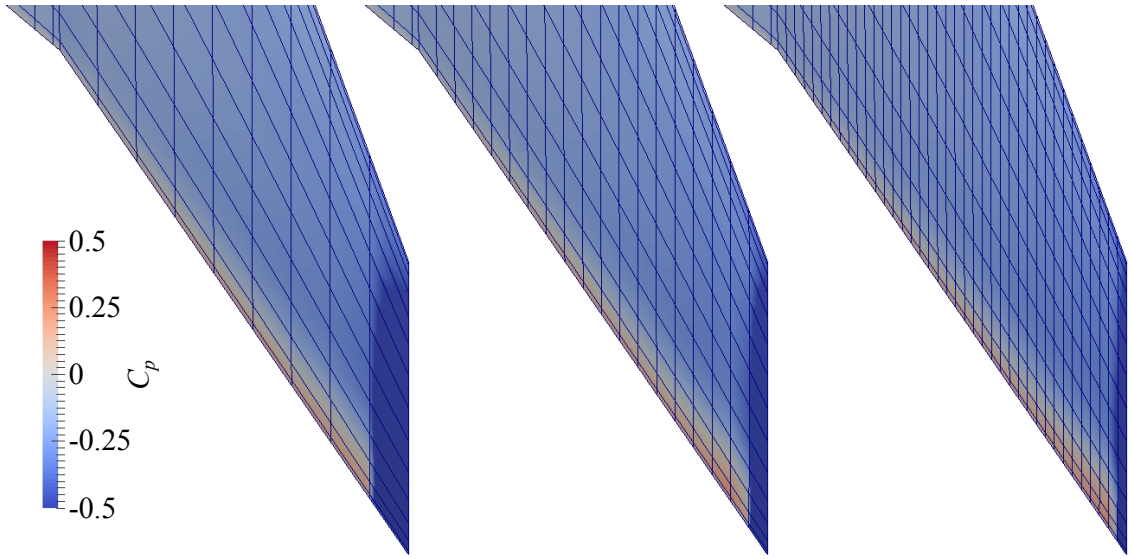

Fig. 5.7: Outboard wing surface pressure with span-wise grid refinement.

Figure 5.8 shows three levels of grid refinement in the chord-wise direction with a constant, cosine spacing of panels in the span-wise direction. With an increase in chord-wise paneling, the shock across the trailing edge is better resolved but, any other changes are hard to see from just the surface contour plot.

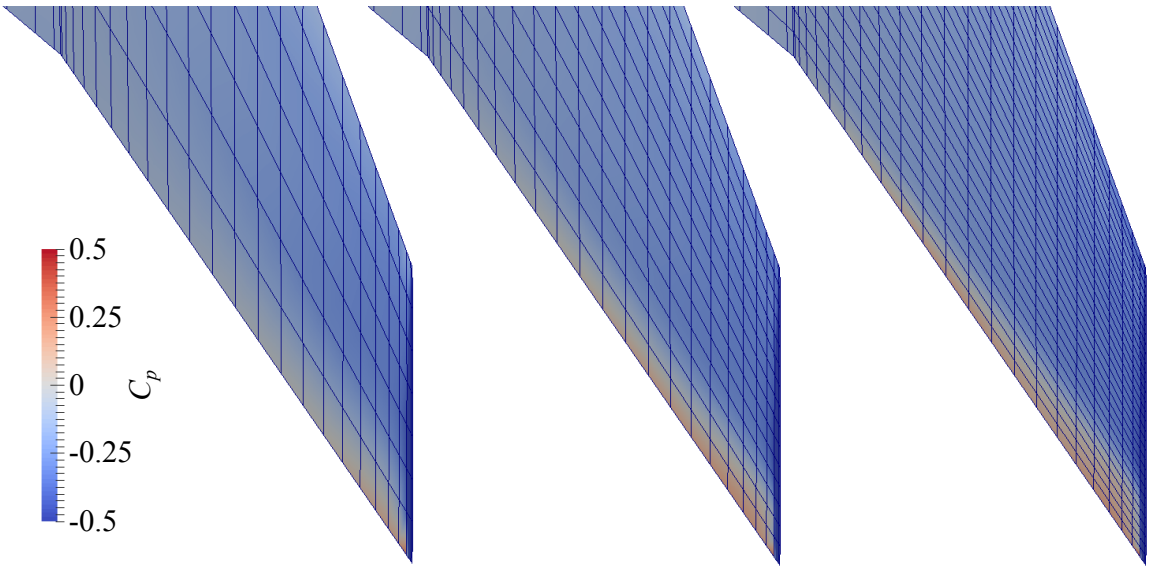

Fig. 5.8: Outboard wing surface pressure with chord-wise grid refinement.

A more quantitative understanding of the effect of grid refinement can be obtained by taking slices at several locations along the wing and plotting the pressure along each slice for different levels of grid refinement. These slices are taken at 6 span wise stations along the wing with each slice running in the chord-wise direction as shown in Fig. 5.9.

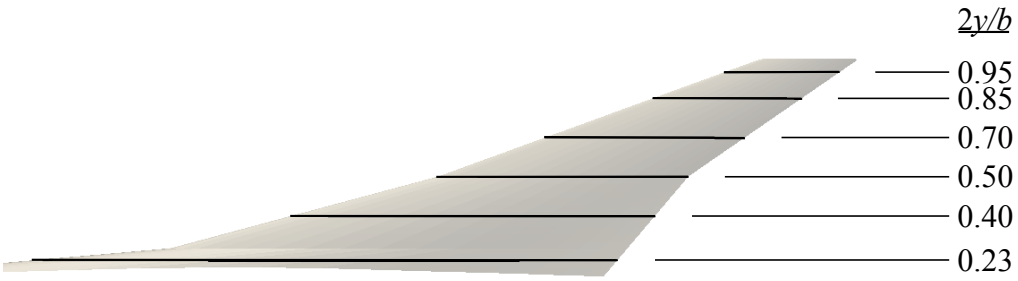

Fig. 5.9: Location of slices along wing for grid convergence and benchmark studies.

Table 5.1: Number of panels used in span-wise portion of grid convergence study.

Mesh	Span-Wise Panels		
	Inner	Middle	Outer
Coarse	2	3	8
Medium	4	6	16
Fine	8	12	32

The span-wise and and chord-wise refinement of the mesh were again treated separately. In the span-wise case, 20 cosine spaced panels were used along the chord. The span-wise paneling was handled based on the three sections of the wing. The spacing in the inner and middle sections of the wing was handled linearly while the spacing on the outer section was clustered towards the tip using half of a cosine distribution. The number of span-wise panels used in the coarse, medium, and fine cases are shown in Table 5.1. The wing tip was capped with a flat network consisting of the same number of chord-wise panels as the wing surface and 5 panels in the other direction. The same flight condition used in the workshop was used here, which consists of a $Mach = 1.6$ and $\alpha = 2.3067°$. The paneling used on the fuselage was kept to a minimal level to allow more refinement on the wing. Coarse paneling on the fuselage is not expected to have a significant effect on the solution of the wing because the nose and middle section of the fuselage are very smooth and well represented with coarse paneling. The tail portion does not influence the wing at all due to its location relative to the wing and the case Mach number.

The results of the span-wise portion of the grid convergence study are shown in Fig. 5.10. Note that the y-axis of the plot has been inverted so that the upper line represents the upper surface of the wing and the lower line the lower surface. It is seen that the solution on the surface of the wing is insensitive to the span-wise paneling even for coarse paneling except near the wing tip. This result should be expected as the strongest gradients in the solution are in the direction of free-stream flow. Additionally, the geometry along the span-wise direction of the wing is smooth.

The final portion of the wing grid convergence study is to repeat the previous exercise except with the span-wise paneling held constant and the chord-wise paneling varied. In

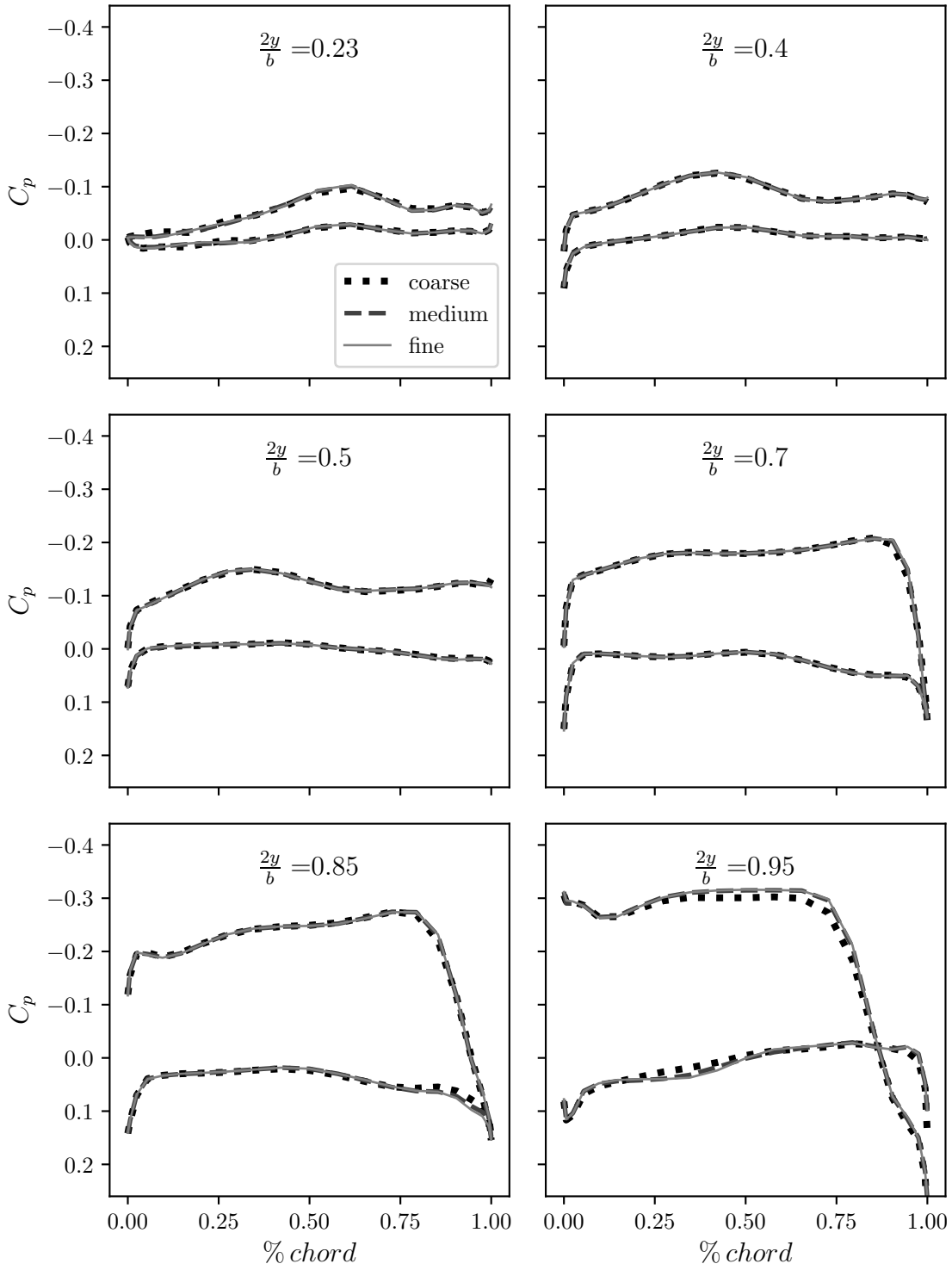

Fig. 5.10: C_p on wing surface vs. span-wise paneling at six span-wise stations.

doing this, the medium level of span-wise refinement specified in Table 5.1 was used with 10, 20, and 40 cosine-spaced panels in the chord-wise direction for the coarse, medium, and fine cases respectively. The wing tip was capped with a flat network consisting of the same number of chord-wise panels as the wing surface and 5 panels in the other direction. Figure 5.11 shows the results for the chord-wise variation in paneling. As expected, it is seen that the solution is more sensitive to the chord-wise paneling.

Several points are learned from looking at grid convergence on the wing. First, the wing solution is fairly insensitive to the span-wise paneling except near the wing tip where very fine span-wise paneling is needed. Using very fine span-wise paneling near the wing tip mitigates the effect of the large pressure spikes at the sharp corners of the tip. Thus, the number of panels needed to effectively resolve the wing can be minimized using a clustering technique like cosine spacing. It was initially thought that additional span-wise refinement is needed at the sharp changes in leading and trailing edge sweep between different sections of the wing. However, this is not true because these sharp changes in geometry are effectively normal to the direction of flow. Second, the wing solution is more sensitive to the chord-wise paneling at the leading and trailing edges where sharp gradients in the pressure usually exist. Cosine spacing can also be used here to cluster points towards these regions.

5.2.3 Benchmark Against Euler Solution

Now that the appropriate level of grid refinement is known, the PANAIR wing solution can be benchmarked in detail against the Euler solution. This benchmark is done by taking slices along the wing at the same locations used in the previous section, see Fig. 5.9, of both the Euler and UNS3D solutions and plotting the results against each other.

The Euler solution was obtained using UNS3D with one of the grids provided by the 2017 AIAA Sonic Boom Prediction Workshop [12]. The grid used contained 6,491,425 control volumes. The UNS3D code has been benchmarked against results from the workshop for the full 25D configuration and was found to be in good agreement [89]. The PANAIR solution used 40 panels along the chord of the wing and 32 along the span. Figure 5.12 shows the surface meshes of PANAIR and UNS3D used for the wing benchmark.

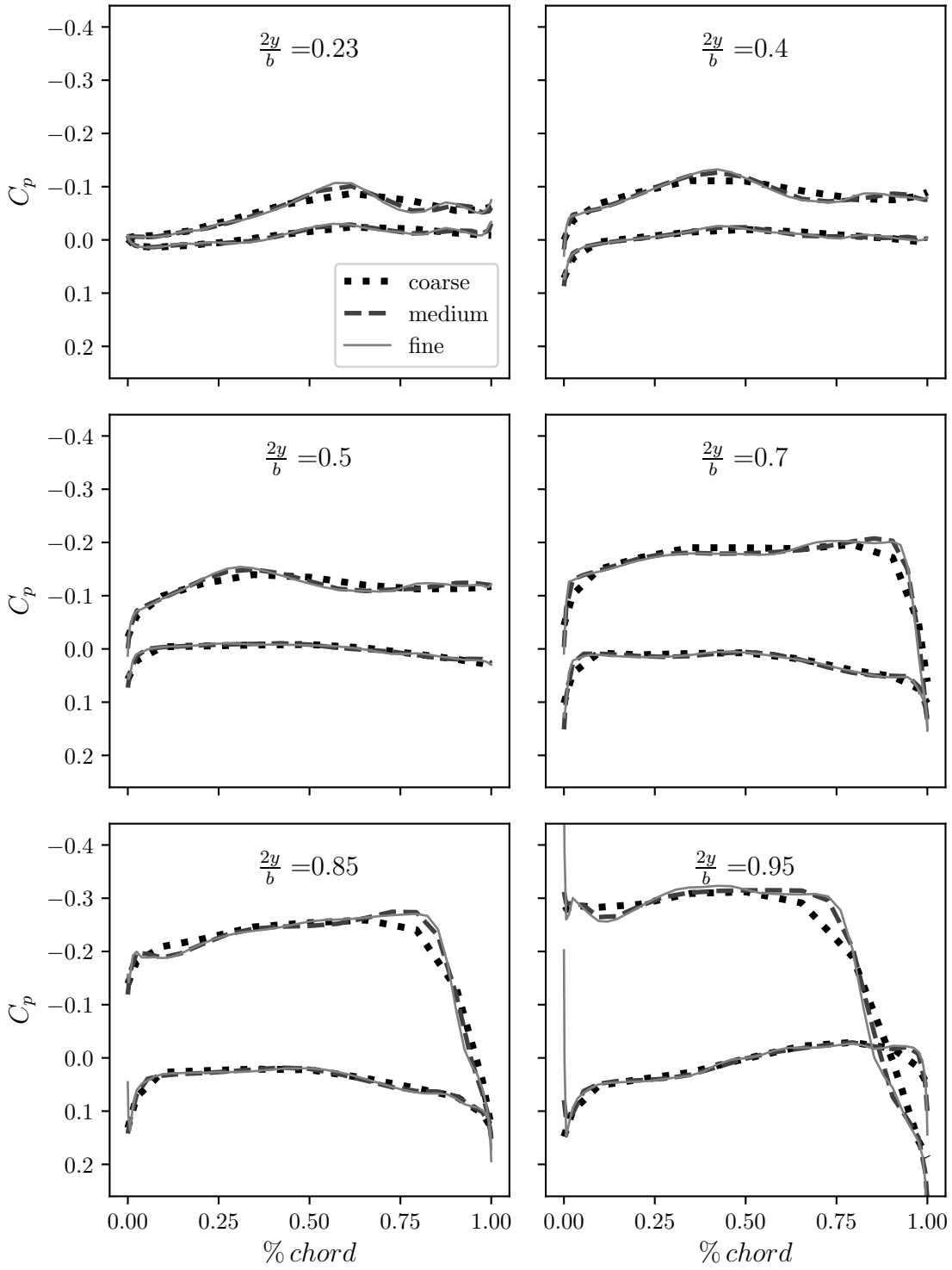

Fig. 5.11: C_p on wing surface vs. chord-wise paneling at six span-wise stations.

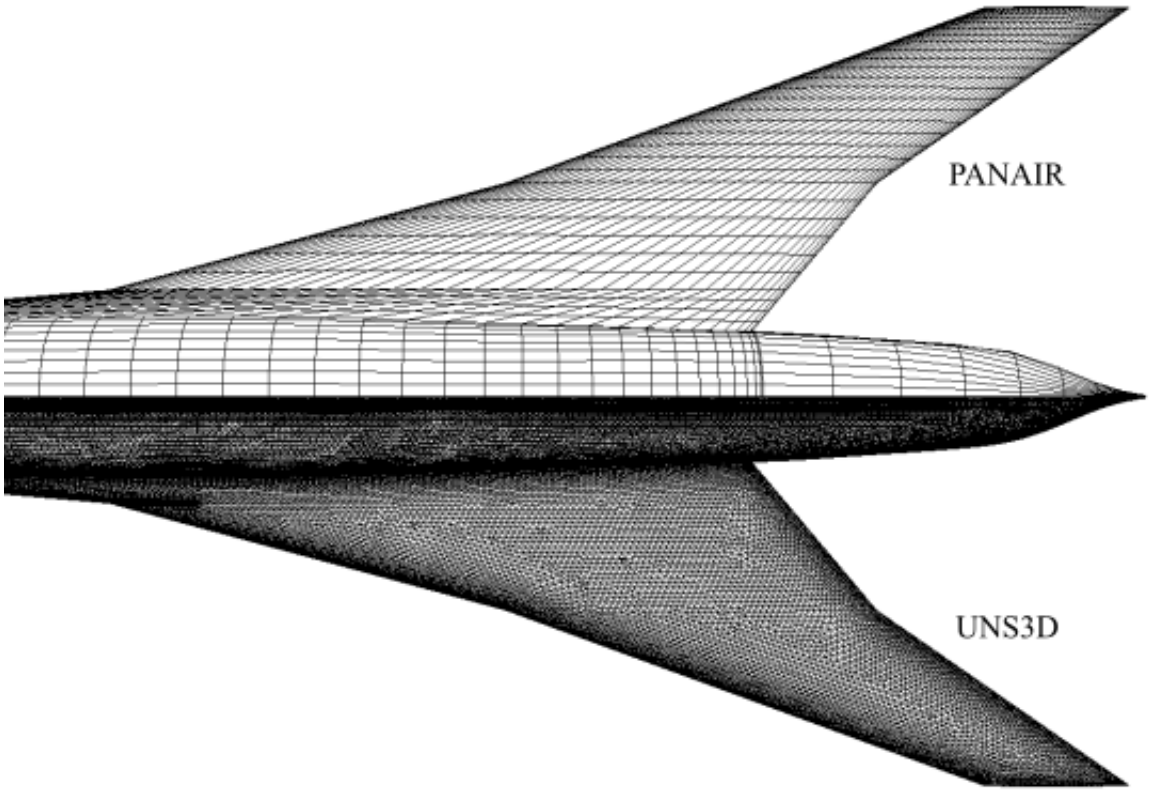

Fig. 5.12: Comparison of PANAIR and UNS3D surface meshes for wing benchmark.

Figure 5.13 shows the results of the benchmark. The PANAIR and UNS3D solutions compare well at the root of the wing but are increasingly different towards the tip of the wing. The primary difference is at the trailing edge of the outboard section of the wing as initially seen in Fig. 5.2. This difference at the trailing edge of the outboard portion of the wing is due to PANAIR using linear characteristics inclined at the freestream Mach angle throughout the solution. Thus, PANAIR predicts a subsonic trailing edge on the outboard portion of the wing when, in reality, the local mach number in this region is higher than the freestream and the trailing edge is supersonic. As a result, PANAIR shows the trailing edge shock on the outboard portion of the wing passing over the down stream portion of the wing. In the non-linear UNS3D solution this shock is inclined further aft of the trailing edge.

The difference in the location of the trailing edge shock can be seen clearly at a lower Mach number where the non-linear solution also predicts a subsonic trailing edge. Figure 5.14 shows contours of the pressure on the top surface of the wing for the PANAIR and UNS3D solutions at $Mach = 1.3$. As expected, the linear panel solution predicts a shock along a linear characteristic aligned at the freestream Mach angle. The non-linear solution shows a curved shock that aligns with the local Mach angle which decreases as the Mach number increases towards the wing tip. Since the higher Mach numbers on the upper surface of the outboard portion of the wing correspond to higher perturbation velocities, it isn't surprising that the linear panel solution, which assumes small perturbation velocities, suffers in this region.

An additional difference between the PANAIR and UNS3D solutions on the wing that should be noted is that the UNS3D solution does not show the large velocities at the wingtip that the PANAIR solution does. Even though the Euler equations being solved by UNS3D are inviscid, there is enough numerical viscosity in the solution that the flow will separate at any sharp corners instead of becoming unrealistically large.

5.3 Fuselage Study

Following the same pattern as was done for the wing, this section will investigate the

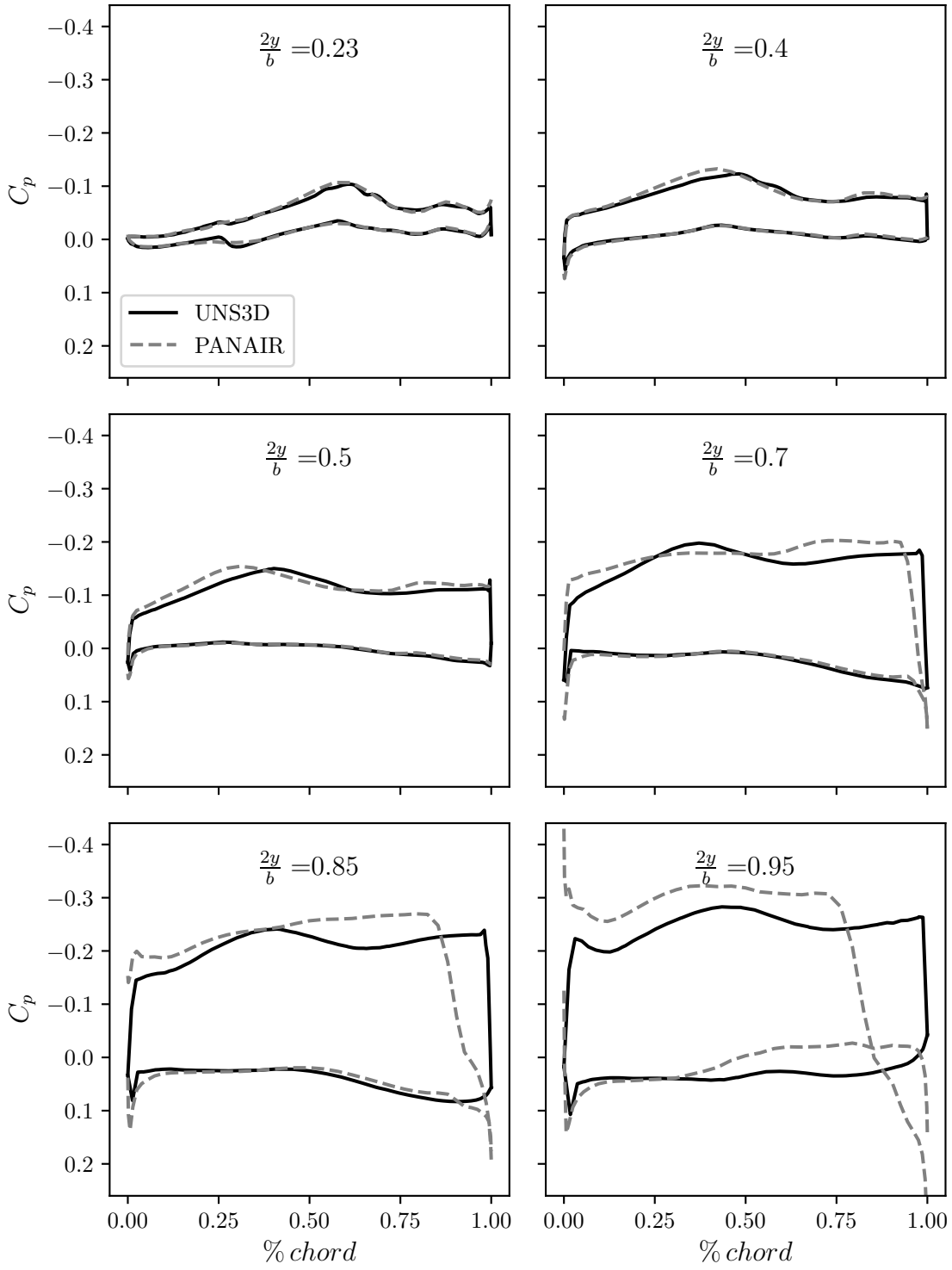

Fig. 5.13: Comparison of PANAIR and UNS3D wing surface pressures.

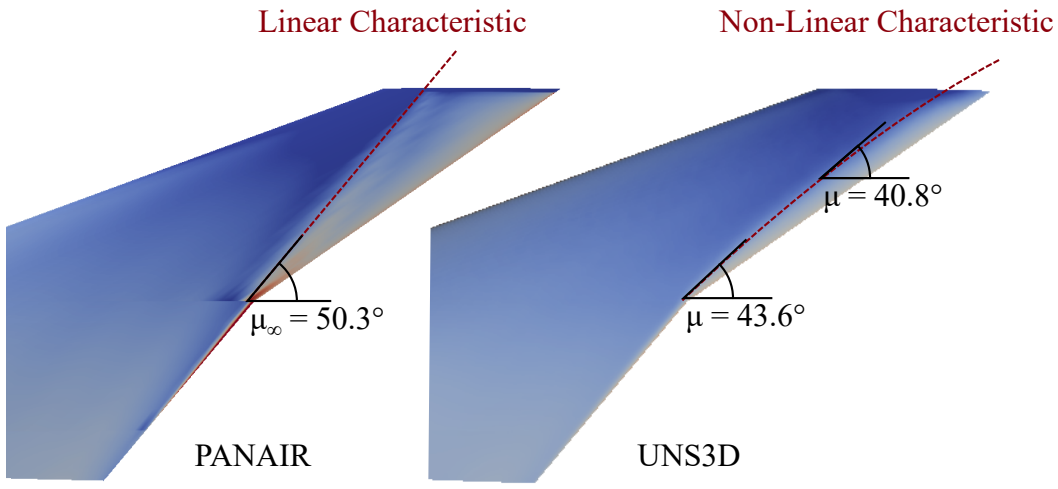

Fig. 5.14: Comparison of outboard wing trailing edge shocks for linear and non-linear solutions at Mach 1.3.

PANAIR solution for the fuselage. The investigation includes checking the validity of the solution, performing grid convergence studies, and benchmarking against the Euler solution.

5.3.1 Solution Check

Based on the preliminary comparisons of the PANAIR and UNS3D results, the tail of the fuselage is the primary area of interest on the fuselage. Similar to the region at the tip of the wing, the corners and higher curvature at the tail test the limits of the linearized supersonic solution. The nose and middle portions of the fuselage appear to match the Euler solution well and will be ignored for the solution check.

The Mach numbers on the tail, as shown in Fig. 5.15, reveal two issues. The first issue is seen on the top of the tail near the end. At this location, there is a small region where the flow Mach number dips below one. Since the linearized supersonic formulation assumes the flow is not transonic or close to transonic, this region is likely to have larger errors. The second issue is seen on the bottom of the tail near the side where there is a large spike in the Mach number. Figure 5.16 shows the magnitude and direction of the velocity vector on the surface using arrow glyphs and lends insight into why this spike in the Mach number occurs. Near the aft region of the tail, there is a cross-flow around the side of the fuselage

from the bottom to the top of the tail. At the point of the spike in Mach number, there is a relatively sharp corner on the side of the fuselage and this, combined with the cross-flow, is resulting in perturbation velocities that violate the assumptions of the linearized solution.

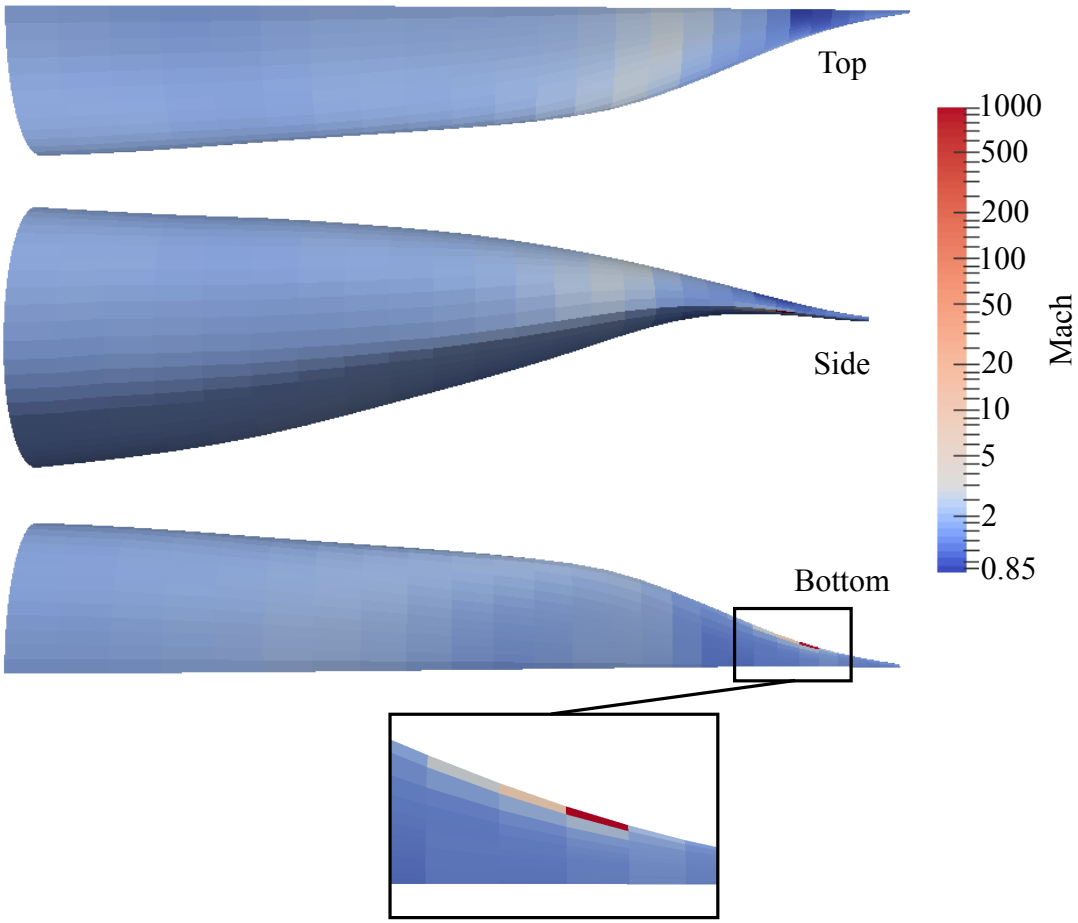

Fig. 5.15: Mach number on surface of fuselage tail.

Figure 5.17 shows the mass flux normal to the surface of the tail. In the same region where there are Mach numbers close to transonic, the PANAIR solution struggles to enforce the boundary conditions of no flow through the surface. Note that, similar to the top of the tail, there is also a recompression shock on the bottom of the tail, see Fig. 5.3. However, this is a weaker shock than on the top and the resulting surface Mach numbers are not transonic. As a result, the linearized solution does not show any issues on the bottom of

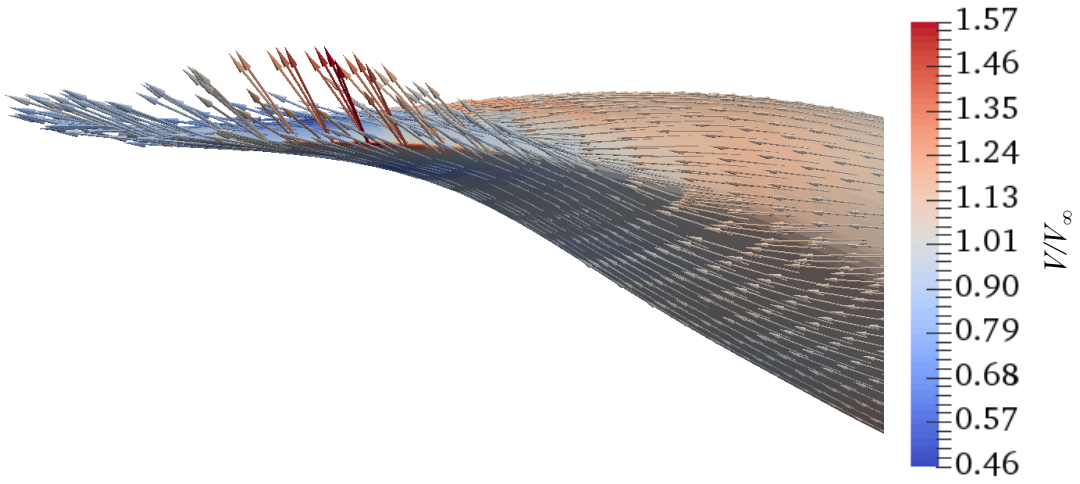

Fig. 5.16: Velocity on surface of fuselage tail.

the fuselage in this region.

While the geometry on the tail may appear relatively smooth to the observer, the solution check has revealed that there are several issues with the linearized solution. The cross-flow around the side of the tail combined with the sharp edge results in unrealistic velocities. Additionally, there is a strong recompression shock near the tip of the tail that results in near transonic Mach numbers that violate the assumptions of the linearized formulation.

5.3.2 Grid Convergence Study

Completing a grid convergence study on the tail was unsuccessful due to large oscillations in the solution on the tip of the tail that appeared as the grid was refined. Figure 5.18 shows the oscillations in the pressure on the surface. The oscillations, which only worsened as additional refinement was added, resulted in the Mach number jumping back and forth between subsonic and supersonic. The oscillations occurred right in and around the location on the tail that has transonic Mach numbers and is likely due to the inability of the panel method to handle transonic flow.

The nose and middle portions of the geometry had no issues with grid refinement and

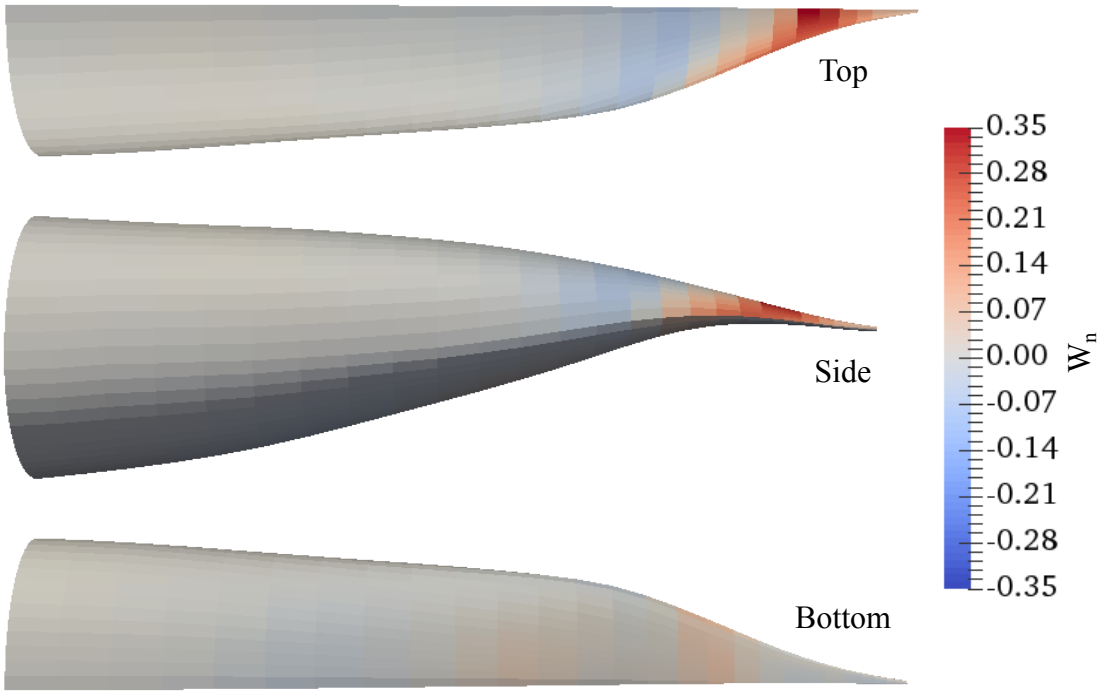

Fig. 5.17: Mass flux normal to surface of fuselage tail.

yielded uninteresting results due to the smoothness of the geometry in these regions. As little as 14 panels that were cosine clustered towards the tip were sufficient to provide a converged solution on the nose. Convergence of the solution around the circumference of the fuselage is very similar to that of the axisymmetric geometry reviewed in the previous chapter.

5.3.3 Benchmark Against Euler Solution

Due to the convergence issues on the tail, it is not possible to compare a fully converged PANAIR solution on the fuselage with the UNS3D solution. However, it was found that using a fairly coarse paneling on the tail in the lengthwise direction avoided the oscillations in the solution and provided the best possible results. Thus, a solution using this coarser paneling on the tail is used to benchmark the fuselage solution. The grid used 14 panels on the nose, 32 panels along the middle portion of the fuselage, and 30 panels around the circumference. The panels on the nose were cosine clustered towards the tip of the nose.

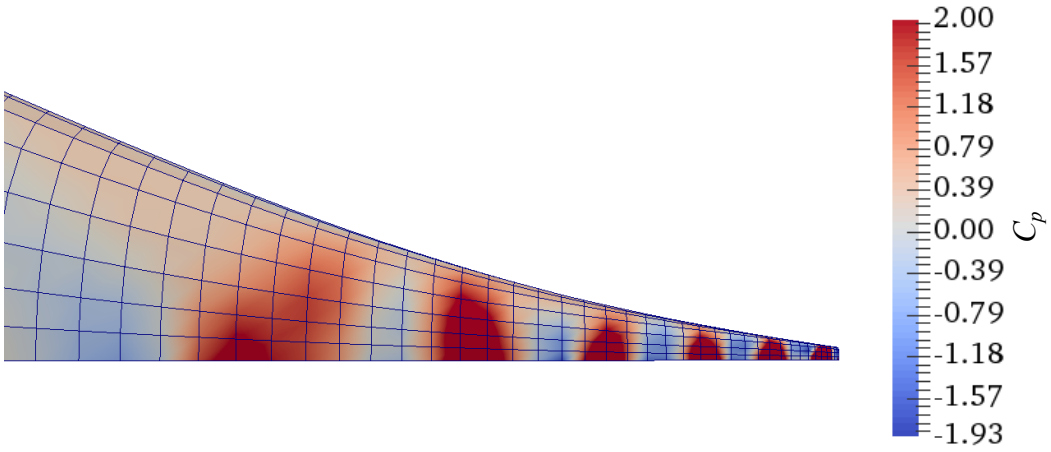

Fig. 5.18: Oscillations in solution of the tail as grid is refined.

Since the paneling on the middle portion of the geometry matches the paneling along the chord of the wing, the middle panels were cosine clustered towards the leading and trailing edges of the wing. The panels in the lengthwise direction on the tail were clustered towards regions of higher curvature. The paneling around the circumference of the geometry was clustered towards the middle of the side to put additional panels on the sharp corner located on the side of the tail. Coarse paneling was used on the wing to allow for additional paneling on the fuselage.

The pressure was compared at slices running lengthwise down the very top and bottom of the fuselage parallel to the plane of symmetry. As shown in Fig. 5.19, the PANAIR solution compares well with the Euler solution along the nose and middle portions of the fuselage. At the tail, the solutions follow a fairly similar trend but the PANAIR solution has larger peaks in both the expansion and the shock on the tail.

5.4 Sonic Boom and Aerodynamic Performance

Now that the PANAIR solution is well understood, another look is taken at the nearfield and ground sonic boom signatures. Results from the grid convergence studies are used to construct the best possible grid. Aerodynamic performance for the design flight condition is also examined and compared against results from the Euler solution.

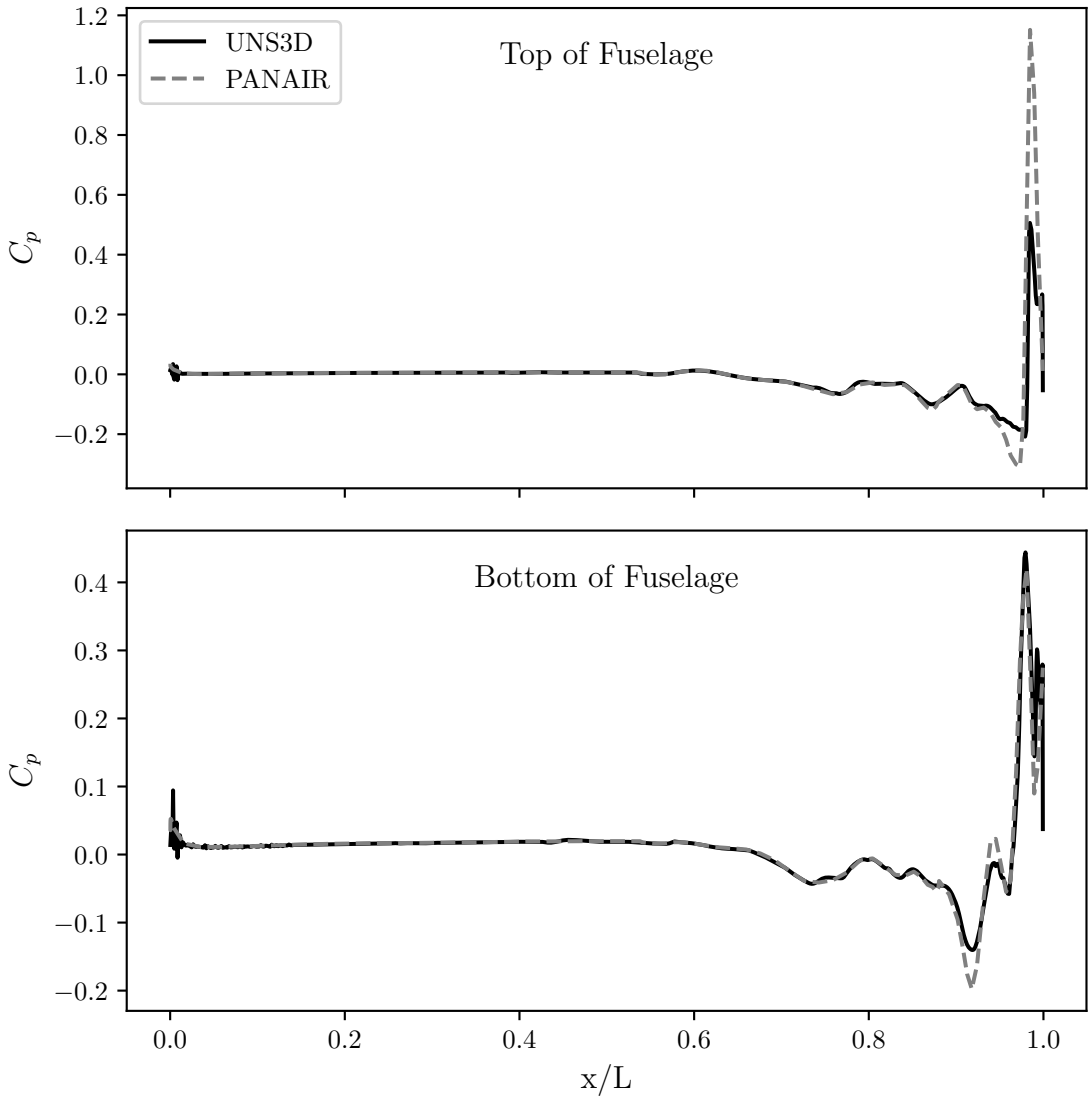

Fig. 5.19: Comparison of PANAIR and UNS3D fuselage surface pressures.

Table 5.2: Comparison of perceived loudness using PANAIR, UNS3D, and CART3D.

	PANAIR	UNS3D	% CART3D
Loudness (PLdB)	86.5	79.9	79.7

The results in this section were generated using a grid similar to that used in the benchmarking of the surface solution. For the wing, 32 panels were used in the chord-wise direction and 4, 6, and 16 panels were used in the span-wise direction for the inboard, middle, and outboard sections respectively. For the fuselage, 30 panels were used around half of the circumference and 13, 32, and 20 panels were used in the length-wise direction for the nose, middle, and tail sections respectively.

Figure 5.20 compares the PANAIR nearfield signature with the Euler nearfield signatures from UNS3D and CART3D. The CART3D results are from the adapted grid solution submitted to the workshop [12] by Lazzara who is a collaborator on the current work. While there are some differences from the preliminary results shown in Fig. 5.1, the PANAIR results still show very large spikes near the end of the signature that are not in the Euler solutions. The end result of these spikes can be seen in the ground signature which is shown in Fig. 5.21 and in the perceived loudness values shown in Table 5.2. The differences between the ground signatures obtained from the PANAIR and Euler solutions do not appear to be as drastic as in the nearfield signature. However, the difference is enough to significantly change the predicted loudness.

It is clear that the axial location of the spikes in the nearfield signature correspond to the axial location of the issues in the surface solution. Based on the analysis of the solution on the aircraft surface, the large spikes in the PANAIR nearfield signature can be attributed to the large over prediction of the magnitudes of the expansion and shock on the the tail.

The lift, drag, and pitching moment coefficients were also computed and are shown in Table 5.3. While the difference in drag is around 6%, the difference in lift and pitching moment is less than 2% and 1% respectively. The small size of these differences is surprising considering how much more computationally inexpensive the panel solution is over the Euler solution. The panel solution performs well in this regard because these performance

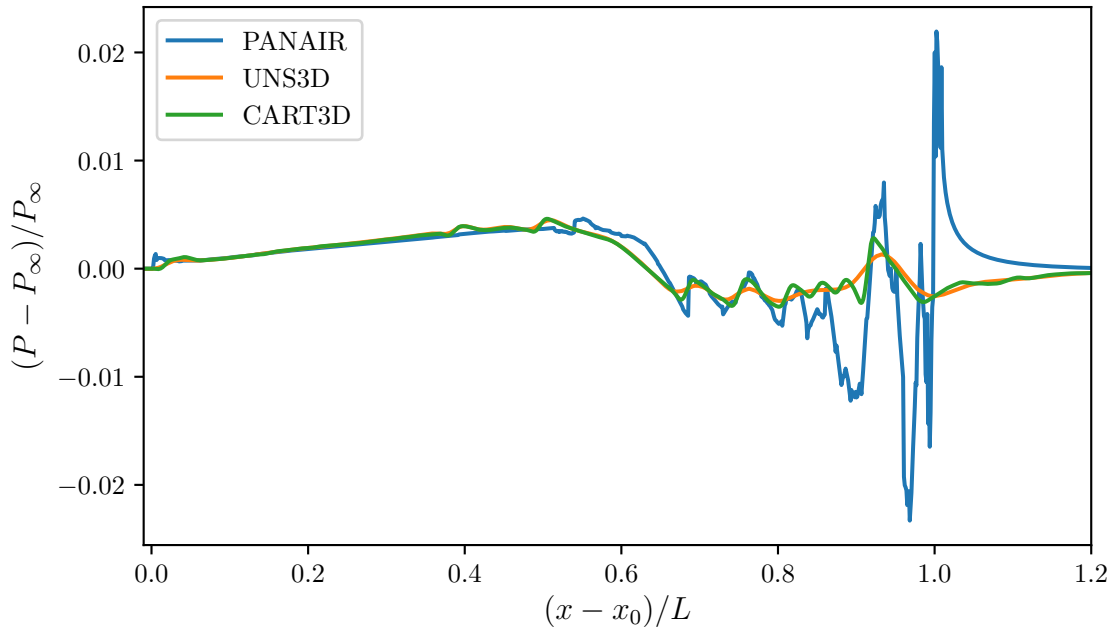

Fig. 5.20: Comparison of PANAIR and UNS3D nearfield pressure signatures at R/L=3.

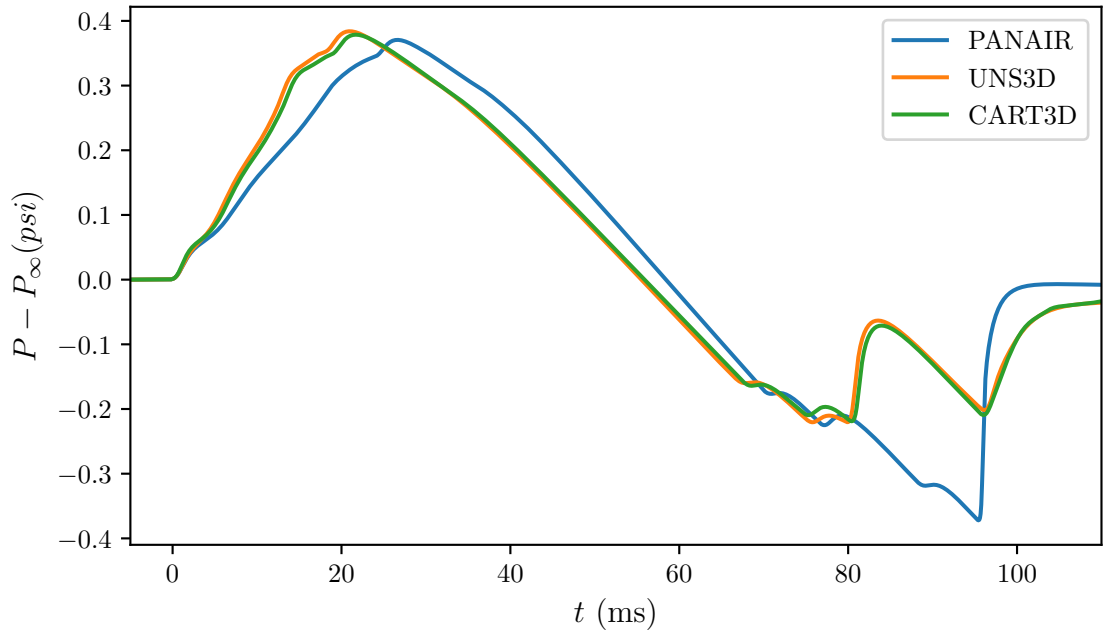

Fig. 5.21: Comparison of PANAIR and UNS3D ground pressure signatures.

Table 5.3: Comparison of PANAIR and UNS3D aerodynamic performance.

	PANAIR	UNS3D	% Error
C_L	0.07893	0.07766	1.6
C_D	0.00661	0.007018	5.8
C_M	-0.06722	-0.06662	0.90

coefficients are integrated quantities and the majority of the panel solution compares well with the Euler solution.

CHAPTER 6

CONCLUSIONS AND FUTURE WORK

The goal of this work is to develop a framework of tools to rapidly predict sonic boom and aerodynamic performance of supersonic transport aircraft using high-order panel methods for the nearfield solution. Panel methods were selected over other low-order techniques based on several papers which showed good results for this application [9, 10, 90]. The framework consisted of CST equations for modeling the aircraft geometry, the panel method PANAIR for obtaining the nearfield solution, sBOOM for the pressure signature propagation, and PyLdB for the calculation of the perceived loudness at the ground. Once finished, the results of the framework were verified and benchmarked against results for axisymmetric and wing-fuselage geometries from the recent 2017 AIAA Sonic Boom Prediction Workshop.

In using the CST equations, the current work sought to take a slightly different approach for surface grid generation than had been used previously. In a similar framework developed by Rallabhandi [10], the surface of each component of the aircraft was meshed individually and then intersections between components were found using a geometry triangulation library. At the beginning of this work, it was thought that the analytical nature of the CST equations would allow for closed form equations for the intersections between surfaces, providing an elegant and alternative solution. However, the nonlinear nature of the CST equations prevented the arrival at a closed form solution. Instead, a simple fixed point iteration method was found to quickly obtain points of intersection at discrete locations and showed good convergence for the surface orientations used. Using this method, techniques and tools were developed to automate the surface mesh generation of a given configuration of surfaces. In addition to using CST surfaces, a more exact representation of the wing-fuselage geometry was obtained using multivariate interpolation. This more accurate representation was desired to remove the error in fitting the CST equations from the benchmark study. Future work will study the effect that the error in the fit of the CST

equations has on the aerodynamic solution. This type of study would provide insight into the number of parameters needed to sufficiently represent the geometry and support future use of these tools in optimization and design.

Verification and benchmarking of the framework of tools developed herein began first with an axisymmetric geometry. This geometry provided a simple starting point to getting all of the tools connected together and understanding the performance of the panel method. Solution convergence with grid refinement was shown as well as the effect of varying the sensor distance. Results showed good agreement with high-fidelity results. Ground signatures were slightly under-aged compared to the non-linear Euler solutions but otherwise similar in shape. These differences between PANAIR and the Euler solutions due to the linearity of PANAIR could likely be corrected in future work using techniques similar to those employed by Chan [9]. Despite slight discrepancies in the pressure signatures, calculated perceived loudness values of the PANAIR and Euler solutions were close and well within one standard deviation of the results submitted to the workshop.

While the axisymmetric results are encouraging, the primary interest is in the ability of panel methods to model the sonic boom of aircraft geometries. A wing-fuselage geometry from the workshop provided a good compromise between the complexity of a full-configuration and incorporating important elements of a real aircraft. Preliminary results for the JAXA wing-body geometry showed large spikes at the tail end of the nearfield signature and observing the nearfield signature provided little insight into the cause. Thus, the primary focus of the verification and benchmarking of the wing-body geometry turned to the solution on the surface. Results of the surface solution showed good agreement with the Euler solution except at the outboard wing and on the tail.

The JAXA wing-body geometry proved to be a very good case for highlighting the shortcomings of PANAIR. Because PANAIR is a potential flow solution, unrealistically large velocities were calculated on the sharp corners at the wing tip and on the side of the tail. The regions affected by the spikes in velocity at the wing tip were shown to be mitigated by increasing panel density at the wing tip. The PANAIR solution also predicted

a shock across the trailing edge of the outboard wing section that did not exist in the Euler solution. This shock is due to PANAIR using linear characteristics oriented at the freestream mach angle, resulting in a subsonic trailing edge. In reality, the flow accelerates enough over the outboard portion of the wing to make the outboard trailing edge supersonic, meaning the Mach number normal to the trailing edge is supersonic. The result of the shock on the trailing edge resulted in pressure values on the outboard portion of the wing that were significantly different from the Euler solution. Despite these issues the solution on the wing was shown to converge with increases in grid refinement. The panel solution on the tail failed to converge with increased paneling. Instead, large oscillations in the solution developed at finer levels of grid refinement and grew worse with increased refinement. These issues arose because the specific shape of the tail results in a small subsonic region on the top of the tail near the tip. As additional refinement is added, the linear panel formulation is unable to resolve the transonic flow. It was found that the best results could be obtained by instead using a coarser grid in this subsonic region on the tail. Comparing the pressure solution of PANAIR on the fuselage to Euler results revealed good agreement along the entire fuselage except at the tail. Although, roughly similar trends were found at the tail between the two solutions, PANAIR largely over predicts the magnitudes of the expansion and following compression shock.

With the surface solution better understood, focus turned again to the nearfield pressure signature. The nearfield and ground signatures generated using PANAIR were compared with those produced using two separate Euler solutions. Despite improvements in the surface paneling, PANAIR still showed large spikes in the tail end of the nearfield signature. These spikes result in large differences in the ground signature and perceived loudness as well. Considering all of the results, it is clear that the issues in the nearfield signature correspond to the issues found at the tail and wingtip of the surface solution. Good agreement is found between the PANAIR and Euler solutions everywhere else. The lift, drag, and pitching moment coefficients obtained using PANAIR were also compared with the UNS3D solution and found to be within 2% error for the lift and moment and 6% error for the drag.

The primary issue encountered in using PANAIR in the present framework is that it may produce good results for most of the solution but then perform very poorly in a few small regions. Although the regions containing poor results are small, the overall accuracy of the sonic boom prediction is greatly diminished. Thus, the challenge is figuring out how the results can still be utilized despite localized regions of poor performance. It may be that the error in the loudness due to, for example, poor results at the aft end of the aircraft can be treated as a systematic error that can be filtered out. Another possibility is that even though the magnitude in the predicted loudness is erroneous, reliable gradients of the loudness with respect to changes in the aircraft shape are still produced for changes in regions where the panel solution is good. In this case, the panel solution could still be directly utilized since the primary input for optimization is gradients of the loudness with respect to changes in design variables and not necessarily loudness magnitudes.

One of the most promising paths forward is to separate the optimization problem into two portions. First, optimal small changes to the baseline nearfield signature or the corresponding equivalent area could be found for expected variations in atmospheric profile and altitude. A second round of optimization could then find the small changes in the OML of the aircraft that produce the optimal changes to the nearfield signature. Approaching it this way, PANAIR could be used to optimize the OML for the portions of the nearfield signature that it models accurately and a higher fidelity tool could be used for the remaining portions of the signature. Another significant advantage to this approach is that the analysis required for the first round of optimization is relatively cheap, allowing for optimal solutions to be explored across a wider range of atmospheres. Trends in these optimal solutions could then be identified to better inform the second round of optimization.

Results from this work have helped illuminate some of the fundamental shortcomings of using high-order panel methods for sonic boom prediction as well as its potential. While the limitations are explicit in the derivation of the method, it is not immediately clear just by looking at a geometry that the assumptions of the formulation will be violated or to what degree the results will be impaired. The results in the current work provide a concrete

example of what can be expected. It should also be noted that, while the sonic boom results obtained for the wing-fuselage geometry were impaired by the specific tail design, everywhere else the PANAIR solution showed good agreement with the Euler solution at a fraction of the cost. Consequently, PANAIR continues to be a compelling option for multi-fidelity work when the number of design variables is large. For preliminary design with basic geometries, panel methods can likely be utilized directly. For more sophisticated designs, panel methods will likely need to be incorporated into multi-fidelity frameworks with higher fidelity tools.

REFERENCES

[1] Federal Aviation Regulations, 14 CFR 91.817, "Civil aircraft sonic boom".

[2] Whitham, G. B., "The Flow Pattern of a Supersonic Projectile," *Communications on Pure and Applied Mathematics*, Vol. 5, No. 3, 1952, pp. 301–348.

[3] McLean, F. E., "Some Nonasymptotic Effects on the Sonic Boom of Large Airplanes," Tech. Rep. NASA-TN-D-2877, 1965.

[4] Maglieri, D. J., Bobbitt, P. J., Plotkin, K. J., Shepherd, K. P., Coen, P. G., and Richwine, D. M., "Sonic Boom: Six Decades of Research," Tech. Rep. NASA/SP-2014-622, Dec. 2014.

[5] Morgenstern, J., Buonanno, M., and Norstrud, N., "N+2 Low Boom Wind Tunnel Model Design and Validation," *30th AIAA Applied Aerodynamics Conference*, 2012.

[6] Ordaz, I., Geiselhart, K. A., and Fenbert, J. W., "Conceptual Design of Low-Boom Aircraft with Flight Trim Requirement," *Journal of Aircraft*, Vol. 52, No. 3, 2015, pp. 932–939.

[7] Kirz, J., "Grid Setups and Numerical Simulations of a Low Boom Concept at Off-Design Flight Conditions," *Deutscher Luft- und Raumfahrtkongres*, 2017.

[8] Lazzara, D. S., Magee, T., Shen, H., and Mabe, J. H., "Off-Design Sonic Boom Performance for Low-Boom Aircraft," *AIAA Scitech 2019 Forum*, 2019, p. 0606.

[9] Chan, M. K., *Supersonic Aircraft Optimization for Minimizing Drag and Sonic Boom*, PhD, Stanford, California, 2003.

[10] Rallabhandi, S. and Mavris, D., "Design and Analysis of Supersonic Business Jet Concepts," *6th AIAA Aviation Technology, Integration and Operations Conference (ATIO)*, 2006, p. 7702.

[11] Choi, S., Alonso, J. J., and Kroo, I. M., "Two-Level Multifidelity Design Optimization Studies for Supersonic Jets," *Journal of Aircraft*, Vol. 46, No. 3, 2009, pp. 776–790.

[12] Park, M. A. and Nemec, M., "Near Field Summary and Statistical Analysis of the Second AIAA Sonic Boom Prediction Workshop," *35th AIAA Applied Aerodynamics Conference*, 2017, p. 3256.

[13] Runyan, L. J. and Kane, E. J., "Sonic Boom Literature Survey. Volume 2. Capsule Summaries," Tech. Rep. FAA-RD-73-129-II, Boeing Commercial Airplane Co. Seattle WA, Sept. 1973.

[14] Runyan, L. J. and Kane, E. J., "Sonic Boom Literature Survey. Volume I. State of the Art." Tech. Rep. FAA-RD-73-129-I, Boeing Commercial Airplane Co. Seattle WA, Sept. 1973.

[15] Plotkin, K. J., "Review of Sonic Boom Theory," *12th Aeroacoustic Conference*, American Institute of Aeronautics and Astronautics, San Antonia, TX, 1989.

[16] Plotkin, K. J., "State of the Art of Sonic Boom Modeling," *The Journal of the Acoustical Society of America*, Vol. 111, No. 1, 2002, pp. 530–536.

[17] Ackeret, J., "Air Forces on Airfoils Moving Faster than Sound," Tech. Rep. NACA-TM-317, 1925.

[18] von Karman, T. and Moore, N. B., "Resistance of Slender Bodies Moving With Supersonic Velocities, With Special Reference to Projectiles," *National Applied Mechanics Meeting of The American Society of Mechanical Engineers*, New Haven, Connecticut, 1932.

[19] Busemann, A., "Aerodynamischer Auftrieb bei berschallgeschwindigkeit," *Luftfahrtforschung*, Vol. 12, No. 6, 1935, pp. 210–220.

[20] Prandtl, L., "Theorie des Flugzeugtragflgels im zusammendrckbaren Medium," *Luftfahrtforsch*, Vol. 13, 1936, pp. 313.

[21] Tsien, H.-S., "Supersonic Flow Over an Inclined Body of Revolution," *Journal of the Aeronautical Sciences*, Vol. 5, No. 12, 1938, pp. 480–483.

[22] Schlichting, H., "Airfoil Theory at Supersonic Speed," Tech. Rep. NACA-TM-897, June 1939.

[23] Puckett, A. E., "Supersonic Wave Drag of Thin Airfoils," *Journal of the Aeronautical Sciences*, Vol. 13, No. 9, 1946, pp. 475–484.

[24] Stewart, H., "The Lift of a Delta Wing at Supersonic Speeds," *Quarterly of Applied Mathematics*, Vol. 4, No. 3, 1946, pp. 246–254.

[25] Hayes, W. D., *Linearized Supersonic Flow*, PhD, California Institute of Technology, 1947.

[26] Carlson, H. W., "An Investigation of Some Aspects of the Sonic Boom by Means of Wind-Tunnel Measurements of Pressures About Several Bodies at a Mach Number of 2.01," Tech. Rep. NASA-TN-D-161, Dec. 1959.

[27] Lina, L. J. and Maglieri, D. J., "Ground Measurements of Airplane Shock-Wave Noise at Mach Numbers to 2.0 and at Altitudes to 60,000 feet," Tech. Rep. NASA-TN-D-235, March 1960.

[28] Smith, H. J., "Experimental and Calculated Flow Fields Produced by Airplanes Flying at Supersonic Speeds," Tech. Rep. NASA-TN-D-621, Nov. 1960.

[29] Lomax, H., "The Wave Drag of Arbitrary Configurations in Linearized Flow as Determined by Areas and Forces in Oblique Planes," Tech. Rep. NACA-RM-A55A18, March 1955.

[30] Walkden, F., "The Shock Pattern of a Wing-Body Combination, Far from the Flight Path," *The Aeronautical Quarterly*, Vol. 9, No. 2, May 1958, pp. 164–194.

[31] Milne, E. A., "Sound Waves in the Atmosphere," *The London, Edinburgh, and Dublin Philosophical Magazine and Journal of Science*, Vol. 42, No. 247, 1921, pp. 96–114.

[32] DuMond, J. W. M., Cohen, E. R., Panofsky, W. K. H., and Deeds, E., "A Determination of the Wave Forms and Laws of Propagation and Dissipation of Ballistic Shock Waves," *The Journal of the Acoustical Society of America*, Vol. 18, No. 1, 1946, pp. 97–118.

[33] Blokhintzev, D., "The Propagation of Sound in an Inhomogeneous and Moving Medium II," *The Journal of the Acoustical Society of America*, Vol. 18, No. 2, 1946, pp. 329–334.

[34] Blokhintzev, D., "The Propagation of Sound in an Inhomogeneous and Moving Medium I," *The Journal of the Acoustical Society of America*, Vol. 18, No. 2, 1946, pp. 322–328.

[35] Keller, J. B., "Geometrical Acoustics. I. The Theory of Weak Shock Waves," *Journal of Applied Physics*, Vol. 25, No. 8, 1954, pp. 938–947.

[36] Groves, G., "Geometrical Theory of Sound Propagation in the Atmosphere," *Journal of Atmospheric and Terrestrial Physics*, Vol. 7, 1955, pp. 113–127.

[37] Rao, P. S., "Supersonic Bangs: Part I," *The Aeronautical Quarterly*, Vol. 7, No. 1, 1956, pp. 21–44.

[38] Rao, P. S., "Supersonic Bangs: Part II," *The Aeronautical Quarterly*, Vol. 7, No. 2, 1956, pp. 135–155.

[39] Whitham, G. B., "On the Propagation of Weak Shock Waves," *Journal of Fluid Mechanics*, Vol. 1, No. 3, 1956, pp. 290–318.

[40] Whitham, G., "A New Approach to Problems of Shock Dynamics. Part I. Two-Dimensional Problems," *Journal of Fluid Mechanics*, Vol. 2, No. 2, 1957, pp. 145–171.

[41] Randall, D. G., "Methods for Estimating Distributions and Intensities of Sonic Bangs," Tech. Rep. R. & M. No. 3113, Aeronautical Research Council, 1959.

[42] Jung, T. P., Starkey, R. P., and Argrow, B., "Modified Linear Theory Sonic Booms Compared to Experimental and Numerical Results," *Journal of Aircraft*, Vol. 52, No. 6, 2015, pp. 1821–1837.

[43] Rallabhandi, S. K., "Advanced Sonic Boom Prediction Using the Augmented Burgers Equation," *Journal of Aircraft*, Vol. 48, No. 4, 2011, pp. 1245–1253.

[44] Pierce, A. D. and Maglieri, D. J., "Effects of Atmospheric Irregularities on Sonic-Boom Propagation," *The Journal of the Acoustical Society of America*, Vol. 51, No. 2, 1972, pp. 702–721.

[45] Darden, C. M., "Limitations of Linear Theory for Sonic Boom Calculations," *Journal of Aircraft*, Vol. 30, No. 3, 1993, pp. 309–314.

[46] Page, J. and Plotkin, K., "An Efficient Method for Incorporating Computational Fluid Dynamics into Sonic Boom Prediction," *9th Applied Aerodynamics Conference*, 1991, p. 3275.

[47] Siclari, M. and Darden, C., "Euler Code Prediction of Near-Field to Midfield Sonic Boom Pressure Signatures," *Journal of Aircraft*, Vol. 30, No. 6, 1993, pp. 911–917.

[48] Cliff, S. E. and Thomas, S. D., "Euler/Experiment Correlations of Sonic Boom Pressure Signatures," *Journal of Aircraft*, Vol. 30, No. 5, 1993, pp. 669–675.

[49] Plotkin, K. and Page, J., "Extrapolation of Sonic Boom Signatures from CFD Solutions," *40th AIAA Aerospace Sciences Meeting & Exhibit*, 2002, p. 922.

[50] Rallabhandi, S. K. and Mavris, D. N., "New Computational Procedure for Incorporating Computational Fluid Dynamics into Sonic Boom Prediction," *Journal of Aircraft*, Vol. 44, No. 6, 2007, pp. 1964–1971.

[51] Ordaz, I. and Li, W., "Using CFD Surface Solutions to Shape Sonic Boom Signatures Propagated from Off-Body Pressure," *31st AIAA Applied Aerodynamics Conference*, 2013, p. 2660.

[52] Ehlers, F. E., Epton, M. A., Johnson, F. T., Magnus, A. E., and Rubbert, P. E., "A Higher Order Panel Method for Linearized Supersonic Flow," Tech. Rep. NASA-CR-3062, 1979.

[53] Ueno, A., Kanamori, M., and Makino, Y., "Multi-fidelity Low-boom Design Based on Near-field Pressure Signature," *54th AIAA Aerospace Sciences Meeting*, 2016, p. 2033.

[54] Hayes, W. D. and Haefeli, R. C., "Sonic Boom Propagation in a Stratified Atmosphere, with Computer Program," Tech. Rep. NASA CR-1299, 1969.

[55] Robinson, L. D., *Sonic Boom Propagation Through an Inhomogeneous, Windy Atmosphere.*, PhD, The University of Texas at Austin, 1991.

[56] Cleveland, R. O., *Propagation of Sonic Booms Through a Real, Stratified Atmosphere*, PhD, The University of Texas at Austin, 1995.

[57] Pilon, A. R., "Spectrally Accurate Prediction of Sonic Boom Signals," *AIAA Journal*, Vol. 45, No. 9, 2007, pp. 2149–2156.

[58] Ozcer, I., "Sonic Boom Prediction Using Euler/Full Potential Methodology," *45th AIAA Aerospace Sciences Meeting and Exhibit*, 2007, p. 369.

[59] Seebass, R. and George, A. R., "Sonic-Boom Minimization," *The Journal of the Acoustical Society of America*, Vol. 51, No. 2C, 1972, pp. 686–694.

[60] Brown, J. and Haglund, G., "Sonic Boom Loudness Study and Airplane Configuration Development," *Aircraft Design, Systems and Operations Conference*, Atlanta, Georgia, 1988.

[61] Needleman, K., Darden, C., and Mack, R., "A Study of Loudness as a Metric for Sonic Boom Acceptability," *29th Aerospace Sciences Meeting*, Reno, Nevada, 1991.

[62] Leatherwood, J. D. and Sullivan, B. M., "Laboratory Study of Effects of Sonic Boom Shaping on Subjective Loudness and Acceptability," Tech. Rep. NASA-TP-3269, 1992.

[63] Leatherwood, J. D., Sullivan, B. M., Shepherd, K. P., McCurdy, D. A., and Brown, S. A., "Summary of Recent NASA Studies of Human Response to Sonic Booms," *The Journal of the Acoustical Society of America*, Vol. 111, No. 1, 2002, pp. 586–598.

[64] Shepherd, L. J. and Sutherland, W. W., "Relative Annoyance and Loudness Judgements of Various Simulated Sonic Boom Waveforms," Tech. Rep. NASA-CR-1192, 1968.

[65] Niedzwiecki, A. and Ribner, H., "Subjective Loudness of N-wave Sonic Booms," *The Journal of the Acoustical Society of America*, Vol. 64, No. 6, 1978, pp. 1617–1621.

[66] Stevens, S., "Perceived Level of Noise by Mark VII and Decibels (E)," *The Journal of the Acoustical Society of America*, Vol. 51, No. 2B, 1972, pp. 575–601.

[67] Fletcher, H. and Munson, W. A., "Loudness, its Definition, Measurement and Calculation," *Bell Labs Technical Journal*, Vol. 12, No. 4, 1933, pp. 377–430, 01719.

[68] Loubeau, A., Naka, Y., Cook, B. G., Sparrow, V. W., and Morgenstern, J. M., "A New Evaluation of Noise Metrics for Sonic Booms using Existing Data," *AIP Conference Proceedings*, Vol. 1685, AIP Publishing, 2015, p. 090015.

[69] Buonanno, M. A., *A Method for Aircraft Concept Exploration Using Multicriteria Interactive Genetic Algorithms*, PhD Thesis, Georgia Institute of Technology, 2005.

[70] Rallabhandi, S. K. and Mavris, D. N., "Aircraft Geometry Design and Optimization for Sonic Boom Reduction," *Journal of Aircraft*, Vol. 44, No. 1, 2007, pp. 35–47.

[71] Rallabhandi, S. K. and Mavris, D. N., "Simultaneous Airframe and Propulsion Cycle Optimization for Supersonic Aircraft Design," *Journal of Aircraft*, Vol. 45, No. 1, 2008, pp. 38–55.

[72] Derbyshire, T. and Sidwell, K. W., "PAN AIR Summary Document (version 1.0)," Tech. Rep. NASA-CR-3250, 1982.

[73] Plotkin, K. J., Downing, M., and Page, J., "USAF Single Event Sonic Boom Prediction Model: PCBOOM," *The Journal of the Acoustical Society of America*, Vol. 95, No. 5, 1994, pp. 2839–2839.

[74] Plotkin, K., Page, J., and Haering, E., "Extension of PCBoom to Over-The-Top Booms, Ellipsoidal Earch, and Full 3-D Ray Tracing," *13th AIAA/CEAS Aeroacoustics Conference (28th AIAA Aeroacoustics Conference)*, 2007, p. 3677.

[75] Bolander, C. R., Hunsaker, D. F., Shen, H., and Carpenter, F. L., "Procedure for the Calculation of the Perceived Loudness of Sonic Booms," *AIAA Scitech 2019 Forum*, 2019, p. 2091.

[76] Song, W. and Keane, A., "A Study of Shape Parameterisation Methods for Airfoil Optimization," *10th AIAA/ISSMO Multidisciplinary Analysis and Optimization Conference*, 2004.

[77] Sripawadkul, V., Padulo, M., and Guenov, M., "A Comparison of Airfoil Shape Parameterization Techniques for Early Design Optimization," *13th AIAA/ISSMO Multidisciplinary Analysis Optimization Conference*, 2010.

[78] Kulfan, B. M., "Universal Parametric Geometry Representation Method," *Journal of Aircraft*, Vol. 45, No. 1, 2008, pp. 142–158.

[79] Leal, P. B. and Hartl, D. J., "Structurally Consistent Class/Shape Transformation Equations for Morphing Airfoils," *Journal of Aircraft*, 2018, pp. 1–12.

[80] Leal, P. B., Giblette, T., Hunsaker, D. F., and Hartl, D. J., "Extended 3D Class/Shape Transformation Equations for Multicomponent Aircraft Assemblies," *AIAA Scitech 2019 Forum*, 2019, p. 0604.

[81] Rockafellar, R. T. and Wets, R. J.-B., *Variational Analysis*, Vol. 317, Springer Science & Business Media, 2009.

[82] Anderson, J. D., *Modern Compressible Flow: With Historical Perspective*, McGraw-Hill, New York, 3rd ed., 2003.

[83] Epton, M. A. and Magnus, A. E., "PAN AIR: A computer program for predicting subsonic or supersonic linear potential flows about arbitrary configurations using a higher order panel method. Volume 1: Theory document (version 3.0)," Tech. Rep. NASA-CR-3251, Nov. 1981.

[84] Kellogg, O. D., *Foundations of Potential Theory*, Dover, 1953.

[85] Ward, G. N., *Linearized Theory of Steady High-Speed Flow*, Cambridge University Press, 1955.

[86] Saaris, G. R., Tinoco, E., Lee, J., and Rubbert, P., "A502I User's Manual-PAN AIR Technology Program for Solving Problems of Potential Flow about Arbitrary Configurations," Tech. Rep. D6-54703, Boeing Commercial Airplane Co. Seattle WA, 1992.

[87] "US Standard Atmosphere, 1976," NASA-TM-X-74335, 1976.

[88] Han, Z.-X. and Cizmas, P. G. A., "A CFD Method for Axial Thrust Load Prediction of Centrifugal Compressors," *International Journal of Turbo & Jet-Engines*, Vol. 20, No. 1, Jan. 2003, pp. 1–16.

[89] Carpenter, F. L., Cizmas, P. G., Reddy, S. R., and Dulikravich, G. S., "Controlling Sonic Boom Loudness Through Outer Mold Line Modification: A Sensitivity Study," *AIAA Scitech 2019 Forum*, 2019, p. 0603.

[90] Choi, S., Alonso, J. J., Kroo, I. M., and Wintzer, M., "Multifidelity Design Optimization of Low-Boom Supersonic Jets," *Journal of Aircraft*, Vol. 45, No. 1, 2008, pp. 106–118.